Article

# How an Inhibitor Bound to Subunit Interface Alters Triosephosphate Isomerase Dynamics

Zeynep Kurkcuoglu,[1] Doga Findik,[1] Ebru Demet Akten,[2] and Pemra Doruker[1,*]
[1]Department of Chemical Engineering and Polymer Research Center, Bogazici University, Bebek, Istanbul, Turkey; and [2]Department of Bioinformatics and Genetics, Faculty of Engineering and Natural Sciences, Kadir Has University, Cibali, Istanbul, Turkey

ABSTRACT The tunnel region at triosephosphate isomerase (TIM)'s dimer interface, distant from its catalytic site, is a target site for certain benzothiazole derivatives that inhibit TIM's catalytic activity in *Trypanosoma cruzi,* the parasite that causes Chagas disease. We performed multiple 100-ns molecular-dynamics (MD) simulations and elastic network modeling (ENM) on both apo and complex structures to shed light on the still unclear inhibitory mechanism of one such inhibitor, named bt10. Within the time frame of our MD simulations, we observed stabilization of aromatic clusters at the dimer interface and enhancement of intersubunit hydrogen bonds in the presence of bt10, which point to an allosteric effect rather than destabilization of the dimeric structure. The collective dynamics dictated by the topology of TIM is known to facilitate the closure of its catalytic loop over the active site that is critical for substrate entrance and product release. We incorporated the ligand's effect on vibrational dynamics by applying mixed coarse-grained ENM to each one of 54,000 MD snapshots. Using this computationally efficient technique, we observed altered collective modes and positive shifts in eigenvalues due to the constraining effect of bt10 binding. Accordingly, we observed allosteric changes in the catalytic loop's dynamics, flexibility, and correlations, as well as the solvent exposure of catalytic residues. A newly (to our knowledge) introduced technique that performs residue-based ENM scanning of TIM revealed the tunnel region as a key binding site that can alter global dynamics of the enzyme.

## INTRODUCTION

Enzyme activity may be linked to conformational flexibility and dynamics, covering broad ranges of length scales and timescales. Thus, hierarchical computational tools, at atomistic and lower resolution, are crucial for complementing experiments in terms of molecular dynamics (MD). Binding of ligands can modify an enzyme's conformational dynamics and thereby cause an allosteric effect on its catalytic activity. Our goal in this computational study was to elucidate the functional dynamics of triosephosphate isomerase (TIM) from the parasite *Trypanosoma cruzi* (TcTIM) within the scope of an inhibitor bound to its interface.

TIM is a crucial enzyme in the glycolytic pathway, which catalyzes the interconversion between dihydroxyacetone phosphate (DHAP) and D-glyceraldehyde 3-phosphate (GAP) by an isomerization reaction without any cofactor or metal ion. Although each identical subunit carries an independent catalytic site, TIM is active in the dimeric form (except in some hyperthermophilic bacteria, where its functional form is tetrameric). However, cooperativity or allostery has not been observed between the two active sites (1). Each subunit (with 251 residues in TcTIM) adopts the TIM-barrel topology, in which the active site is located at the C-terminal end of the $\beta$-barrel. Four catalytic residues (Asn-12 and Lys-14 on loop 1, His-96 on loop 4, and Glu-168 on loop 6) are shown on the x-ray structure 1tcd (2) in Fig. 1 *a*. Catalytic loop 6 (Glu-168-P178), loop 7 (Gly-212-Lys-218), and loop 8 (Gly-235-Lys-240) also contribute to the active-site geometry via hydrogen (H)-bonding interactions with the substrate (3). Interdigitating loop 3 (Gln-66-Val-79) plays a crucial role in the stability of the dimer by interacting with the other subunit (4–6).

The functional loop 6 (shown in open conformation in Fig. 1 *a*) closes over the substrate and protects it from solvent exposure during catalysis. The specific closed state of loop 6 during formation of the substrate-enzyme complex is stabilized by the interaction between this so-called phosphate-gripper loop and the substrate phosphodianion (7). However, this loop closure is not ligand gated (8), i.e., its opening/closure has been observed in MD simulations on apo TIM (9) and its complex with DHAP (10). In fact, there are some crystal structures (e.g., 1tsi (11) and 1lzo (12)) in which loop 6 is in an open conformation despite the presence of the ligand on the catalytic site. NMR studies have suggested that loop 6 motion is partially rate limiting in the interconversion between DHAP and GAP (13). Previous computational studies, including both coarse-grained elastic network modeling (ENM) and classical MD simulations (9,10,14–17), have indicated that the loop dynamics are coupled with the global modes of TIM, which can be identified as counterrotation and bending of subunits. Similar coupling has been observed in other enzymes with functional loops (17), suggesting

*Submitted March 2, 2015, and accepted for publication June 8, 2015.*

*Correspondence: doruker@boun.edu.tr

Editor: Ivet Bahar.



0006-3495/15/09/1169/10

http://dx.doi.org/10.1016/j.bpj.2015.06.031

that the global modes of such enzymes enable or facilitate the functional loop motions.

Subunit interfaces of oligomeric enzymes, including TIM, may serve as species-specific drug target sites that are especially important for parasitic diseases (4) since they are generally less conserved than the active site (4,18,19). Several benzothiazole derivatives have been reported as candidate drugs against Chagas disease because they inhibit TcTIM's activity (5,19,20). One such inhibitor, referred to as bt10 (Fig. 1 *b*), binds to the specific tunnel region at TcTIM's interface (5,19). Previous works revealed that bt10 interacts with the aromatic clusters formed by Phe-75 of one subunit and Tyr-102/103 of the other subunit on the interface (21–23) in the tunnel region formed by dimerization. Our previous blind docking study (23) indicated that bt10 binds selectively to the tunnel region in the dimer, whereas its specificity for the interface decreases in the monomer. However, the specific inhibitory mechanism of this derivative is still not clear. Previous studies suggested that it leads to destabilization of the interface upon binding and subsequent dissociation into monomers (21,22). On the other hand, the MD simulations presented here show that the interface region occupied by bt10 enhances the network of interactions and at the same time modifies the overall dynamics of the protein. As such, there seems to be an allosteric effect on the catalytic site and loop 6.

Our aim in this work was to elaborate on the nature of this allosteric effect in action. Specifically, we monitored changes in the conformational dynamics on local and global scales by comparing multiple MD simulations of apo and complex structures and ENM. Mixed coarse-grained ENM (MCG_ENM), where the ligand is shown in atomistic detail and the protein is coarse-grained at the residue level, was found to be suitable for vibrational-dynamics analyses of numerous conformations spanned during the MD simulations. Finally, we introduce an ENM methodology in which we scan all residues of dimeric TIM one by one by placing extra nodes at side-chain heavy atoms, to assess each residue's effect on the collective dynamics. Interestingly, the tunnel region emerges as the most significant one in terms of constraining the global modes.

## MATERIALS AND METHODS

### MD simulations

We carried out six independent 100-ns-long runs for apo and bt10-bound TcTIM (three for each) using AMBER9 (24) with ff03 force-field parameters (25). We obtained the force-field parameters for the ligand (a benzothiazole derivative, 2-2(2-(4-aminophenyl) benzothiazole)-6-methyl-benzothiazole-7-sulfonic acid, sodium salt) using the antechamber module of AMBER after determining the restrained electrostatic potential (RESP) partial charges using Gaussian 03 (26) at the B3LYP/6-31+G** level. Apo runs were based on the x-ray structure with Protein Data Bank (27) ID 1tcd (2) at 1.83 Å resolution. For TcTIM-bt10 complex simulations, we used bt10-docked structures from our previous docking study (23). The detailed configurations of each run are given in Table S1 in the Supporting Material.

Energy minimization initially was performed using 500 cycles of the steepest-descent algorithm and then switched to the conjugate gradient, with convergence of the root mean-squared (RMS) gradient per atom being 0.01 kcal/mol/Å. Initial velocities were assigned according to the Maxwellian distribution at 10 K and the temperature was gradually increased to 300 K.

We performed NPT (with isotropic position scaling) simulations at 300 K and 1 atm using a truncated octahedron periodic box with dimensions of ~90 Å, filled with TIP3P water molecules (28) and neutralized with $Cl^-$ ions. To dissipate heat homogeneously, Langevin dynamics was applied for the first 1 ns with a collision frequency of 1 $ps^{-1}$. Later, the weak-coupling algorithm (29) was applied for both temperature and pressure with a default relaxation time constant of 1 ps each. We set the time step to 2 fs by using the SHAKE algorithm (30). For long-range electrostatic interactions, the Ewald summation technique with the particle-mesh method (31) was used with a cutoff distance of 9 Å. Snapshots were recorded every 10 ps, amounting to 9000 frames excluding the equilibration period (10 ns) for each run.

### Principal component analysis

To extract the essential or dominant anharmonic modes for each run, we performed a principal component analysis (PCA) using a covariance matrix based on the $C^{\alpha}$ coordinates of the aligned snapshots (32). Based on the cumulative effect of the first five PCs or PCs that contributed to 90% of total motion, we calculated orientational cross-correlation maps that gave the cosine of the angle between fluctuation vectors of residue pairs. The cross correlations varied in the range of −1 to 1, with the lower and upper limits indicating fully anticorrelated and correlated fluctuations in terms of orientation, respectively, and zero indicating uncorrelated fluctuations.

### Clustering of MD snapshots

All MD runs, including apo and complex, were clustered together based on loop 6 or four active-site residues (Fig. 1 *a*) after each subunit was aligned independently. Clustering of snapshots at 100 ps intervals (5400 snapshots) was performed with respect to mutual RMS deviation (RMSD) values using the *k*-means clustering algorithm implemented in the kclust module of MMTSB Ensemble Tools (33).

### Overlap between eigenvector subspaces

$O(i,j)$ gives the absolute value of the inner product between any two eigenvectors with mode indices $i$ and $j$:

$$O(i,j) = \left| u_i^A . u_j^B \right|, \tag{1}$$

where $u_i$ is the $i^{\text{th}}$ eigenvector from either PCA or ENM. It is a unit vector of dimensions $3N$ for a protein of $N$ residues. Superscripts $A$ and $B$ indicate the different eigenvector sets from either independent MD runs or ENM modes of different snapshots. An overlap value equal to one indicates a perfect match between the directions of the displacement vectors for all nodes. Overlap matrices are plotted for all $(i,j)$ pairs between two different eigenvector sets.

### MCG_ENM to assess the ligand's effect on collective dynamics using MD snapshots

MCG_ENM (34) was previously introduced as a modified version of classical ENM (35,36) that allows one to model protein complexes as a combination of high-resolution (atomistic) and low-resolution (coarse-grained at residue and even higher levels) nodes to attain atomistic detail and

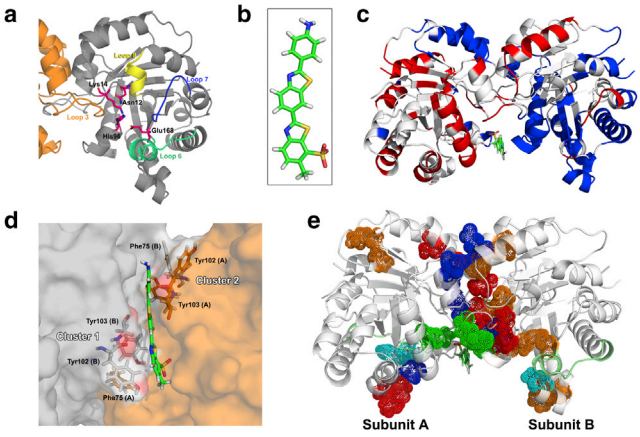


FIGURE 1 Structure, interactions, and residue mobility of dimeric TcTIM. (*a*) Four catalytic residues (*magenta sticks*) and neighboring loops are shown on one of the identical subunits of TcTIM (1tcd). Catalytic loop 6 (*green*, in open conformation) closes over the active site and protects the substrate from solvent exposure during catalysis. Interdigitating loop 3 is important for the stability of the dimer. (*b*) Structure of the inhibitor bt10, a benzothiazole derivative. (*c*) Residues whose MSFs change upon bt10 binding by >20% compared with apo runs are colored. Subunit A expresses increased MSF (*red residues* on the left monomer), whereas subunit B mobility is mostly constrained (*blue*) in the presence of ligand. (*d*) The inhibitor lies in the tunnel-shaped cavity at the subunit interface and interacts with two identical aromatic clusters. (*e*) Binding of the inhibitor changes the H-bonding network in the protein. Residue pairs with marked changes are shown in dot representation: red, increased H-bonds by 20%; orange, 15–20% increase; blue, 20% decrease; cyan, 15–20% decrease. Arg71 (A), Lys-113 (A), and Tyr-103 (B) that interact with the $SO_3^-$ group of the inhibitor are indicated in green.To see this figure in color, go online.

computational efficiency at the same time. In this work, we found this approach to be especially suitable for investigating the collective dynamics of protein-ligand complexes. For this purpose, we took the coordinates of all of the ligand's heavy atoms into account and modeled the protein at low resolution (i.e., coarse-grained at the residue level) by placing nodes at the residue centroids. In the high-resolution region, each heavy atom has unit mass, and pairs of atoms that fall within a specified cutoff radius (7 Å) are connected by identical harmonic springs with a force constant of unity. In the low-resolution region, the force constant between any two coarse-grained nodes is equal to the total number of heavy atom pairs (from two different residues) that fall within the same atomistic cutoff. The mass of each coarse-grained node is equal to the number of heavy atoms it has.

On each MD snapshot (54,000 in total), we performed MCG_ENM to extract the slowest eigenvectors and eigenvalues, which represent the global mode shapes and their squared frequencies, respectively. As a result, we were able to determine the effect of ligand binding on the mode shapes and frequencies by comparing apo and complex runs.

### Residue-based scanning to reveal effective regions on collective dynamics

Here, we introduce a new (to our knowledge) method based on standard (residue/$C^{\alpha}$-based) ENM, where the side-chain heavy atoms of a specific residue are included as extra nodes to mimic and pronounce the presence of a ligand that may interact with that specific site/residue. We scan the residues of the protein one by one by taking each residue's heavy atoms as extra nodes. A residue-based cutoff distance of 15 Å is used between all pairs of nodes, whether they include the backbone $C^{\alpha}$ of each residue or the specific residue's side-chain atoms. Thus, the effect of side chains is overemphasized here.

For each scanned residue, we calculate the percentage shift in the $i^{th}$ collective mode's eigenvalue ($\lambda_i$) as

$$\%shift\ for\ mode\ i\ =\ \frac{\lambda_i(modified)-\lambda_i(original)}{\lambda_i(original)}(x100), \tag{2}$$

where $\lambda_i$ (original) is from standard ENM (nodes at $\alpha$-carbons) and $\lambda_i$ (modified) is from ENM, where a specific residue's side-chain atoms are also included. The % shift value for each residue is then calculated as an average over the 10 slowest modes. In this way, we seek to detect the locations/residues that cause the highest shifts in the frequencies of the collective modes.

## RESULTS AND DISCUSSION

### RMSDs and residue mean-square fluctuations

The RMSDs of MD snapshots with respect to the minimized initial structure of each run are confined within 2.5 Å, indicating stability over 100 ns (Fig. S1). The potential and kinetic energy profiles (not shown) equilibrate within the first 1–2 ns of each run. Based on the RMSD profiles of dimer and monomers, the first 10 ns of each run were discarded as the equilibration period from further analysis.

Residue mean-square fluctuations (MSFs) were calculated for apo and bt10-bound TIM, and are shown in Fig. S2 for each run. Two-way ANOVA was applied on residue-based MSFs, with the null hypothesis that the ligand has no effect on the residue MSF. The null hypothesis was rejected with a $p$ value of 0.0185 (<0.05). We show the change in MSF values upon ligand binding in Fig. 1 *c*. If the MSF of any residue in the complex increased (decreased) by >20% with reference to the apo runs, it is shown in red (*blue*) based on the average over three runs. In the presence of bt10, the residue's mobility increased in subunit A, whereas it decreased in subunit B. This effect is due to the asymmetric shape of bt10 and its interactions with the enzyme considered next.

### Specific interactions

To gain insight into intra- and intermolecular interactions, we analyzed $\pi$ stacking and H-bonding in the presence and absence of the ligand bt10. We first concentrated on two identical aromatic clusters (Fig. 1 *d*) at the interface formed by Phe-75 of one subunit and Tyr-102/103 of the other subunit, which have been reported to be important for the stability of the dimer (19,21,22). These clusters are located at the ends of the tunnel-shaped region in the interface (Fig. 1 *d*). It has been proposed that benzothiazole inhibitors bound to this region destabilize the aromatic clusters, eventually leading to disruption of the dimer and inactivation of the enzyme (21,22). The inhibitor bt10 interacted with the aromatic clusters throughout our MD runs.

Contrary to the disruption hypothesis, our $\pi$-$\pi$ distance analysis indicates that binding of the ligand enhances the stability of the aromatic clusters. Table 1 summarizes the percentages of intact $\pi$-$\pi$ interactions within these clusters during the simulations. Here, the criterion for interaction is taken as the distance between two aromatic rings' centroids being $<7$ Å (37). It can be seen that $\pi$ stacking is enhanced more in cluster 1. A slight decrease is observed between Tyr-102 (A) and Tyr-103 (A) (cluster 2), but still both aromatic clusters are stable when the ligand is bound. Tyr-103 of both subunits predominantly interacts with the ligand, as shown in Fig. 1 *d*.

The total number of H-bonds between subunits A and B, which is calculated as an average over all snapshots, increases from $6 \pm 2$ in apo to $7 \pm 2$ in complex runs. There are $1 \pm 1$ additional H-bonds between the inhibitor and interface residues in each snapshot. Specifically, the $SO_3^-$ group of bt10 mostly interacts with Arg-71 (A), Lys-113 (A), and Tyr-103 (B) (shown in *green* in Figs. 1 *e* and S3). These findings also confirm the stability of the dimeric structure in the presence of ligand.

We further investigated changes in the H-bonding network of the enzyme upon ligand binding. If the occurrence of H-bonds between any two residues increased or decreased by $>15\%$, those residues are colored in Fig. 1 *e* (see detailed lists in Table S2 and Fig. S3). In particular, H-bonding between the subunits was influenced, and this effect propagated toward loop 6 of both subunits. H-bonds were enhanced mostly toward subunit B, which may explain the reduced MSF values of the same subunit.

Three loop 3 residues of subunit A (Thr-76, Gly-77, and Glu-78) exhibit increased H-bonds with their partners from subunit B when bt10 is bound. It has been stated that each Thr-76 contributes to the H-bonding network of the other subunit's active site (3). Intersubunit H-bonding between Thr-76 and the catalytic residue Asn-12 is present in ~10% of the snapshots, and we do not observe a significant change in the complex. Instead, there is an enhancement in H-bonding between Thr-76 (A) and Glu-98 (B). As for catalytic loop 6, the occurrence of H-bonding increases for the Ser-97-Glu-168 pair on subunit B and decreases for Thr-171-Trp-175 on subunit A.

Overall, the increase in the number of both intersubunit $\pi$-$\pi$ interactions and H-bonds indicates a stronger interaction network, i.e., a constrained region at the interface, which will be shown to affect the collective dynamics significantly.

**TABLE 1 Percentage of Intact $\pi$-$\pi$ Interactions in Apo and Complex Runs**

| Aromatic Cluster | $\pi$-$\pi$ Pair | Apo | Complex |
|---|---|---|---|
| 1 | Phe-75 (A)-Tyr-102 (B) | 43 | 95 |
| 1 | Phe-75 (A)-Tyr-103 (B) | 95 | 90 |
| 1 | Tyr-102 (B)-Tyr-103 (B) | 22 | 66 |
| 2 | Phe-75 (B)-Tyr-102 (A) | 79 | 96 |
| 2 | Phe-75 (B)-Tyr-103 (A) | 85 | 91 |
| 2 | Tyr-102 (A)-Tyr-103 (A) | 70 | 53 |

## Collective dynamics and frequency shifts

### *PCA of MD runs*

We first applied PCA on each trajectory to extract the essential anharmonic modes (PCs) of motion for the apo and complex forms. In our previous MD and ENM studies (9,10,14,17), counterrotation of the subunits (Figs. S4 and 2 *a*) appeared as a common, global mode that drove loop 6 opening/closure over the active site in apo TIM of two different species, namely, chicken and *Trypanosoma cruzi*. In this work, this mode can also be detected among the first three or four PCs of the apo and complex runs (Fig. S4). Another common PC describes the bending of the subunits. Details of the PCA are summarized in Fig. S4 and Table S3. Residue cross-correlation maps (based on the cumulative action of the first five PCs or $>100$ PCs that contribute to 90% of total motion) in Figs. S5 and S6 indicate that the strength of correlations for certain regions decreases in the presence of bt10.

### *Convergence of collective modes*

Our 100-ns-runs are not long enough for us to observe the convergence of collective motions. Because different regions of the conformational space are sampled in each run (not shown here), there is no clear one-to-one correspondence between independent runs, as displayed in the overlap matrices in Fig. S4. In fact, the convergence of PCA in MD simulations has been examined for various proteins (38–42) and found to be problematic unless the sampling time approaches the longest relaxation times (on the order of microseconds or longer).

On the other hand, ENM is commonly used to extract the global vibrational modes of proteins (36,43). Due to its computational efficiency, ENM may be preferable to long MD simulations in terms of providing full convergence of collective modes (44), such as in the case of G-protein-coupled receptors. Therefore, in this study, for the first time to our knowledge, we apply the mixed coarse-grained version of ENM, where the ligand is modeled at atomistic resolution, to quantify the ligand's effect on the collective dynamics of TIM more clearly. There is a reasonable level of similarity between the MCG_ENM modes based on the average structure of each run and the PCs in Fig. S7. If the slowest ENM modes extracted from the average structure of different MD runs are compared with each other, there is almost a one-to-one correspondence, indicating convergence of the collective modes (Fig. S8).

### *MCG_ENM analysis of MD snapshots*

For a complete analysis of the trajectories, we performed MCG_ENM on each MD snapshot to extract its slowest harmonic modes, which we then further evaluated using

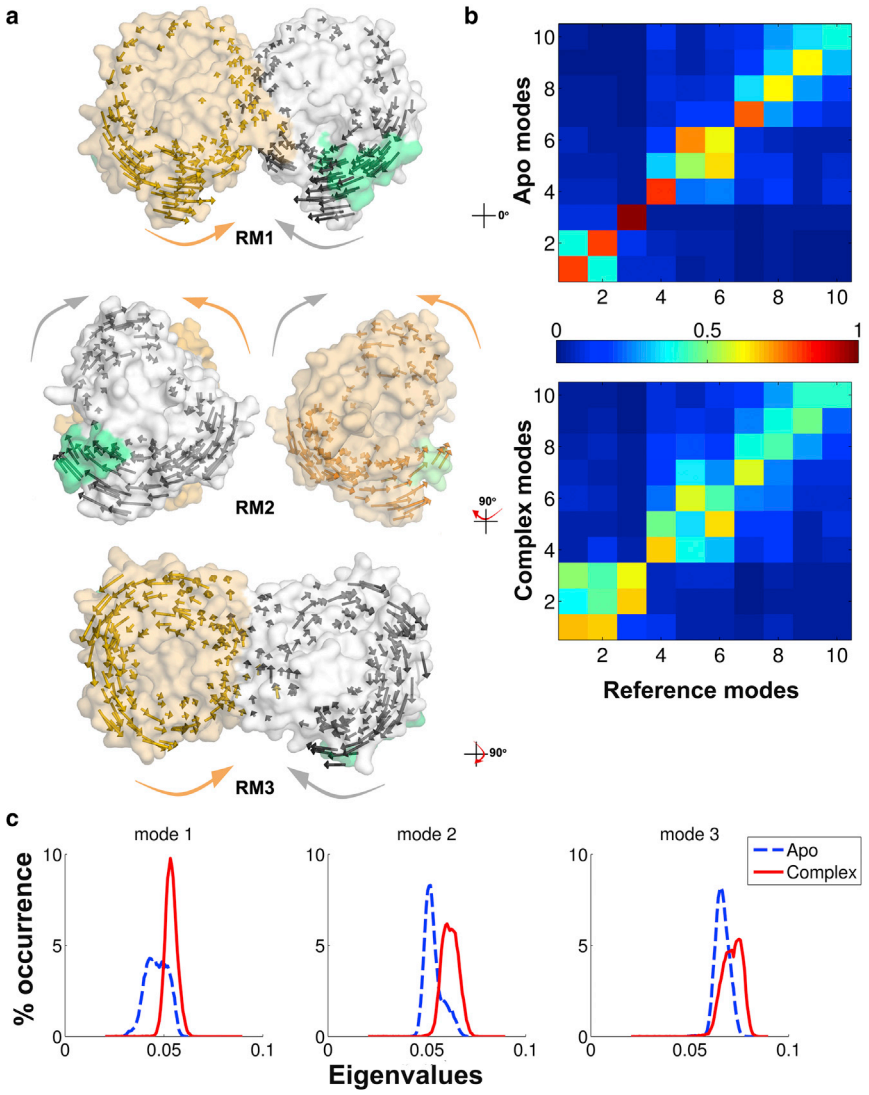


FIGURE 2 Effect of the ligand on collective modes from MCG_ENM. (*a*) RMs extracted from Apo1 (snapshot at the 10th ns) are shown in vector representation (subunits distinguished as surfaces in *white and light orange*, loop 6 in *green*). RM1: bending of the subunits (front view); RM2: counterrotation of subunits coupled with loop 6 opening/closure; and RM3: another bending-type motion observed from the top. (*b*) Overlap matrix between the RMs and the ENM modes extracted from apo and complex runs (snapshots). Each matrix represents an average over the ENM modes of 27,000 snapshots. In particular, the first four modes are conserved throughout all apo simulations. In contrast, both scattering and a decrease in the overlap values are observed in the complex. (*c*) Eigenvalue distributions of the apo and complex snapshots for the first three modes. In all cases, binding of the ligand introduces a restraint on the collective dynamics (i.e., shifts the frequencies to the right). To see this figure in color, go online.

overlap matrices. We used the ENM modes of the 10th-ns snapshot of the Apo1 run (i.e., after the equilibration period) as reference modes (RMs) in our calculations, as shown in Fig. 2 *a*. Here, RM1 represents bending of the subunits, which is denoted as the front view. RM2 is the counterrotation (twisting) of the subunits, which is coupled to catalytic loop opening/closure (shown in side views). RM3, another bending-type motion, is shown from the top after the dimer was rotated 90° with respect to the front view. The RMs closely resemble the ENM modes of the crystal structure 1tcd, as shown in Fig. S9 a. Specifically, the starting structures of other apo and complex runs also originate from the initial stages of the Apo1 run (see Table S1 for details), which indicates that the 10th-ns snapshot of Apo1 run is an appropriate reference.

The extent of one-to-one correspondence between the first 10 eigenvectors of any MD snapshot (apo or complex) with the RMs of the Apo1 initial structure is shown in Fig. 2 *b*. Each entity of the overlap matrix represents an average over all of the MD snapshots considered (total of 27,000 snapshots for either apo or complex; see Fig. S9 for overlaps of individual runs). The first four RMs are almost always preserved in apo simulations (average overlap values $>$ 0.95). In contrast, the overlap values with RMs decrease significantly in the complex and there is a scattered behavior rather than a one-to-one correspondence. These observations in the complex are due to alterations in mode shapes and/or swapping among the slowest modes (see Table S4 for details on this issue). In contrast to the preservation of the first four modes in apo simulations, RM1, RM2, and RM4 (not shown) cannot be observed in 25–30% of the snapshots in the complex. RM3, on the other hand, is highly conserved even in the presence of the inhibitor.

The eigenvalue distribution based on all snapshots of the apo or complex runs are shown in Fig. 2 *c*. The distributions are plotted separately for the first three global modes without considering the effects of mode swapping or character changes. The aim here is to observe whether the global

modes' vibrations are constrained or relaxed by the ligand, which may imply stability or the onset of instability in the dimeric structure, respectively. When the ligand is bound to the interface, the first three slowest modes' eigenvalues (squared frequencies) indicate significant shifts to the right. Thus, the inhibitor seems to act as a constraint on the global modes of the protein, i.e., there is no implication of dissociation. Inasmuch as it has been shown that global modes are coupled with catalytic loop dynamics, we expect that major loops, especially those surrounding the active site (including loop 6), should be influenced by bt10.

## Catalytic loop 6 dynamics

In this section and the next, we aim to reveal any allosteric effects (namely, changes in the catalytic region's conformational dynamics) due to ligand binding. Loop 6 opening/closure events have been monitored by the distance between $\alpha$-carbons of the loop 6 tip residue (Gly-174) and a relatively immobile residue, Tyr-211, at the beginning of loop 7 (9,10,45). In our current apo and complex runs, multiple opening and closure events of the loop are observed during 100 ns (Fig. S10). Fig. 3 *a* gives normalized distributions for the Gly-174-Tyr-211 distance, which indicate a wider range (9.5–21 Å) being sampled in complex runs than in apo (13–20 Å).

We assessed the flexibility of loop 6 by calculating its pseudo-dihedral angles in apo and complex runs. The $i^{\text{th}}$ pseudodihedral angle connecting residues $i$ and $i + 1$ is calculated based on the $C^{\alpha}$ coordinates of residues $i - 1$, $i$, $i + 1$, and $i + 2$. Both curves in Fig. 3 *b* give RMS fluctuations of pseudo-dihedral angles averaged over chains A and B. Previously, N- and C-terminal residues (P169-W171 and K177-A179, respectively) were detected as hinges that drive rigid-lid closure upon binding of the substrate, based on a comparison of one apo and one bound crystal structure (46). Here, however, the loop flexibility in the apo state is apparent in the tip and C-terminal

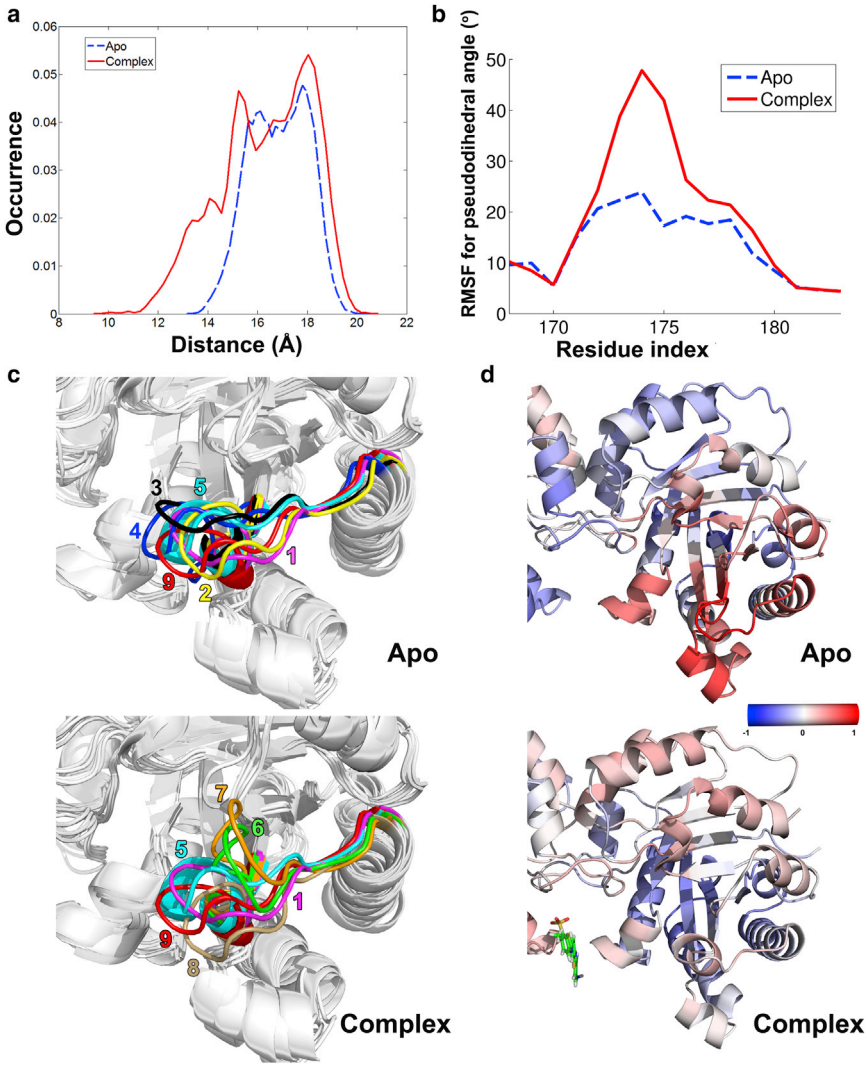


FIGURE 3 Catalytic loop 6 dynamics. (*a*) Distance between the loop's tip residue Gly-174 and a relatively immobile residue, Tyr-211. In the complex, loop 6 samples more closed conformers. (*b*) RMSD for pseudodihedral angles on loop 6 including N-terminal (P169-W171), tip (A172-G176), and C-terminal (K177-A179) residues. The presence of the inhibitor especially increases the flexibility of the catalytic loop's tip residues. (*c*) Clustering based on a mutual RMSD for loop 6 of subunit B. A flip on the tip is observed in cluster 6-7, which contains complex structures. The cluster numbers are given beside the loop conformations in conformity with Fig. S11. (*d*) Color-coded orientational correlations between loop 6 tip residues (Ile-173-Thr-175) and other regions in subunit B. The presence of the ligand affects the coordination of loop 6 with other regions, especially with loop 7-8 around the active site. To see this figure in color, go online.

residues, in conformity with previous computational and NMR studies (9,10,45,47,48). In the presence of the inhibitor, the loop's tip residues (especially Ile-173, Gly-174, and Thr-175) become even more flexible.

Interestingly, the clustering of loop 6 conformers (separately for subunits A and B) indicates a segregation of the apo and complex snapshots (Fig. S11), which implies allosteric changes in the catalytic loop due to bt10 binding. The clusters for subunits A and B are presented in Figs. S11 and Fig. 3 *c*, respectively. In the presence of bt10, the loop explores some distinct conformations in both subunits, where a flip of its tip is observed (cluster 6-7 in Fig. 3 *c*) corresponding to the lower range of the Gly-174-Tyr-211 distance in Fig. 3 *a*.

The orientational correlations of loop 6 tip residues with other regions are given in Fig. 3 *d* for subunit B, and in Figs. S5 and S6 for subunit A. The coordination of the catalytic loop with other regions is clearly affected by the presence of ligand. In particular, the positive correlations of loop 6 with loops 7 and 8, emphasized in terms of functional relevance in a recent study by Katebi and Jernigan (48), decrease in the complex.

## Effect on catalytic residues

Even though bt10 located at the tunnel does not directly interact with the catalytic residues, the solvent-accessible surface area (SASA) values of Asn-12, His-96, and Glu-168 significantly decrease in the complex (Fig. 4 *a*). We calculated all SASA values by using a probe atom of 1.4 Å radius with the SASA module of the VMD visualization tool (49). This effect seems to be in accordance with the sampling of more closed conformers of loop 6 (Fig. 3 *a*), and both results suggest reduced access to the catalytic residues in the complex.

Further clustering of snapshots based on four catalytic residues reveals that apo and bt10-bound conformers belong to different clusters for each subunit (Fig. S12). In subunit B, snapshots from the complex runs tend to group in cluster 4 (*yellow*) and segregate from the apo snapshots. This is in line with the constraining effect of the ligand on the MSF. The difference between clusters is mostly emphasized by the positioning of Glu-168 in both subunits as shown in Fig. 4 *b*.

## The tunnel is a key region for constraining collective modes

As explained in the Materials and Methods section, we locally placed extra nodes at the heavy side-chain atoms of a residue and calculated the resulting average shift in the eigenvalues of the 10 slowest modes (Eq. 2). After scanning all residues of the TIM dimer, we colored the residues according to their effect on the eigenvalues (Fig. 5). Red residues are those that act as significant constraints on the system, thereby shifting the collective mode frequencies to the right (increasing the vibrational frequencies). Blue residues correspond to solvent-exposed protruding loops or chain ends, which shift the eigenvalues to the left when extra masses are included.

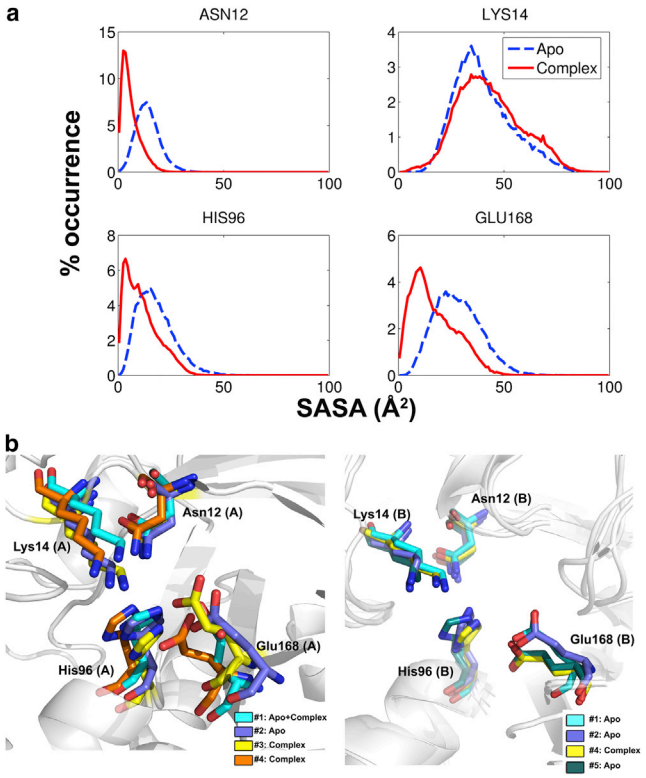


FIGURE 4 Conformational dynamics of catalytic residues Asn-12, Lys-14, His-96, and Glu-168. (*a*) SASA distributions based on all apo and complex snapshots. Binding of bt10 leads to significant reductions in the SASA of all catalytic residues except Lys-14. (*b*) Main clusters of apo and complex snapshots, using a mutual RMSD of 1.5 Å for catalytic residues (see Fig. S12 for cluster details). Glu-168 displays the most variability. To see this figure in color, go online.

Through this analysis, the tunnel region shows distinguishably positive shifts in eigenvalues. Tyr-102 and Tyr-103, which form the aromatic clusters, are the top-ranking residues in this respect. Thus, binding of a ligand to the tunnel region is expected to restrict the collective dynamics of TIM and may therefore alter the enzyme's function. For instance, the tunnel has a more significant effect than other regions at the interface (shown in three different views). The implications of this method in terms of detecting important allosteric sites at the interface of other multimeric enzymes need to be assessed.

## CONCLUSIONS

Through MD simulations and ENM, we were able to observe the allosteric effects of an inhibitor bound to the TIM interface on the dynamics of the catalytic site and loop, which can be further linked to the enzyme's collective

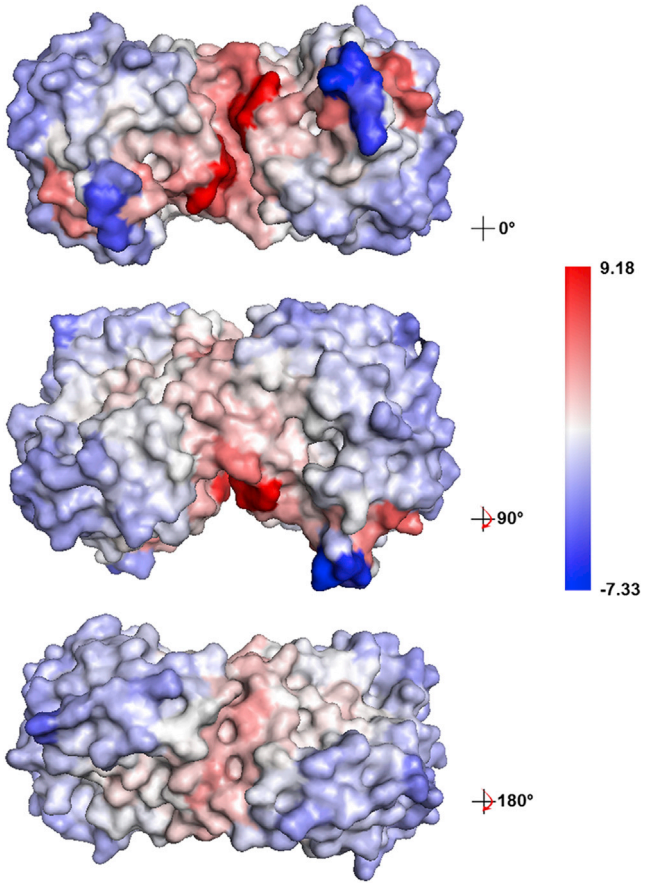


FIGURE 5 Residue-based scanning reveals that the tunnel region has the greatest effect on the collective dynamics. Three different points of view show the tunnel at the interface, the catalytic site (front view), and from the top. The molecule is colored according to the average % shift in first 10 eigenvalues. The top-ranking residues are Tyr-102 and Tyr-103 in the aromatic clusters. To see this figure in color, go online.

dynamics. The inhibitor bt10 stabilizes aromatic clusters at the dimer interface and enhances intersubunit H-bonding at the same time. Thus, we speculate that bt10 inhibition should be realized through an allosteric effect on the catalytic site rather than by destabilization of the dimeric structure, as proposed previously in the literature (21,22). However, we cannot rule out the possibility of observing the dissociation of the dimer on much longer timescales (microseconds and above) than that studied here.

Small molecules that interfere with protein-protein interactions have been categorized according to their mode of action (orthosteric inhibition, allosteric regulation, or interfacial binding/stabilization) (50–52). Orthosteric inhibitors bind at the dimeric interface and inhibit dimerization, whereas allosteric inhibitors bind to a region other than the interface and occlude the binding of their partners, such as BRaf inhibitors that block the Braf-CRaf complex (53). The third category includes molecules that bind to the interface, stabilize the complex, and at the same time produce an allosteric effect on activity. One example is the dead-end complex of ADP-ribosylation factor (ARF) and Sec7-domain-containing ARF exchange factors due to brefeldin A binding (50). In this study, we found that bt10 binds to the tunnel region, which is at the edge of the interface, and its effect seems to propagate through the H-bonding network toward the active site. Moreover, in our previous blind docking study (23), 89% of bt10 poses were located in the tunnel region of the TIM dimer, whereas comparatively fewer (38%) tended to be located in the interfacial region of monomeric TIM. In view of these findings, bt10 seems to fall into the third category due to its stabilization of the dimeric structure and its allosteric effect on the active region's conformational dynamics.

The global modes (i.e., counterrotation and bending of the subunits) appear to be altered significantly by the inhibitor. Moreover, the vibrational frequencies of these modes shift to the right, emphasizing a constraining effect that seems to propagate from the interface to the active site. Thus, significant changes in the dynamics, flexibility, and correlations of the catalytic loop are observed together with reductions in the SASA of catalytic residues. As such, these changes may potentially hinder substrate entrance, substrate positioning in the active site, and/or product release steps.

In this work, we used the MCG_ENM approach for the first time (to our knowledge) to study the collective dynamics of protein-ligand complexes. Because of its computational efficiency, we were able to perform MCG_ENM on all of the MD snapshots (54,000 conformers) and quantify the effect of ligand binding on the vibrational dynamics. This method takes into account all heavy atoms of the ligand and therefore represents intermolecular interactions better than the case of assigning an arbitrary coarse-grained node(s) for the ligand. MCG_ENM may also be helpful for quantifying the extent to which alternative ligand positions alter functional modes.

The so-called tunnel region at the interface of TIM represents a key site for modifying its conformational dynamics on global and local scales. Scanning of residues by modifying the side chains also indicates that constraining this specific region significantly changes the global vibrational modes. Along this line, the scanning methodology introduced here is being assessed in terms of its utility to determine sites for allosteric regulation/inhibition.

Overall, this study suggests that the binding of ligands to key sites at subunit interfaces may act as a constraint for the folded network of interactions and thereby affect enzyme dynamics and function. Especially in the case of enzymes with functional loops, ligands may modify the coupling between global and loop dynamics, with potential effects on the catalytic steps.

## SUPPORTING MATERIAL

Twelve figures and four tables are available at http://www.biophysj.org/biophysj/supplemental/S0006-3495(15)00614-1.

## AUTHOR CONTRIBUTIONS

Z.K., E.D.A., and P.D. designed research. Z.K. and D.F. performed research and analyzed data. D.F., Z.K., and P.D. developed computational methods. Z.K., D.F., E.D.A., and P.D. wrote the manuscript.

## ACKNOWLEDGMENTS

We thank Bulent Balta for helping with the force-field parameterization of bt10 and the MD setup, and Osman Teoman Turgut for discussions about constraints on oscillatory systems.

This work has been partially supported by The Scientific and Technological Research Council of Turkey (TÜBİTAK, Project No: 109M213) and Bogazici University BAP (Project No: 9360).

## REFERENCES

1. Schnackerz, K. D., and R. W. Gracy. 1991. Probing the catalytic sites of triosephosphate isomerase by 31P-NMR with reversibly and irreversibly binding substrate analogues. *Eur. J. Biochem.* 199:231–238.
2. Maldonado, E., M. Soriano-García, …, R. Perez-Montfort. 1998. Differences in the intersubunit contacts in triosephosphate isomerase from two closely related pathogenic trypanosomes. *J. Mol. Biol.* 283:193–203.
3. Wierenga, R. K., E. G. Kapetaniou, and R. Venkatesan. 2010. Triosephosphate isomerase: a highly evolved biocatalyst. *Cell. Mol. Life Sci.* 67:3961–3982.
4. Perez-Montfort, R., M. T. de Gomez-Puyou, and A. Gomez-Puyou. 2002. The interfaces of oligomeric proteins as targets for drug design against enzymes from parasites. *Curr. Top. Med. Chem.* 2:457–470.
5. Téllez-Valencia, A., S. Avila-Ríos, …, A. Gómez-Puyou. 2002. Highly specific inactivation of triosephosphate isomerase from *Trypanosoma cruzi*. *Biochem. Biophys. Res. Commun.* 295:958–963.
6. Olivares-Illana, V., A. Rodríguez-Romero, …, A. Gómez-Puyou. 2007. Perturbation of the dimer interface of triosephosphate isomerase and its effect on *Trypanosoma cruzi*. *PLoS Negl. Trop. Dis.* 1:e1.
7. Zhai, X., M. K. Go, …, J. P. Richard. 2014. Enzyme architecture: the effect of replacement and deletion mutations of loop 6 on catalysis by triosephosphate isomerase. *Biochemistry.* 53:3486–3501.
8. Williams, J. C., and A. E. McDermott. 1995. Dynamics of the flexible loop of triosephosphate isomerase: the loop motion is not ligand gated. *Biochemistry.* 34:8309–8319.
9. Cansu, S., and P. Doruker. 2008. Dimerization affects collective dynamics of triosephosphate isomerase. *Biochemistry.* 47:1358–1368.
10. Kurkcuoglu, Z., and P. Doruker. 2013. Substrate effect on catalytic loop and global dynamics of triosephosphate isomerase. *Entropy (Basel).* 15:1085–1099.
11. Verlinde, C. L., C. J. Witmans, …, F. R. Opperdoes. 1992. Structure of the complex between trypanosomal triosephosphate isomerase and N-hydroxy-4-phosphono-butanamide: binding at the active site despite an "open" flexible loop conformation. *Protein Sci.* 1:1578–1584.
12. Parthasarathy, S., G. Ravindra, …, M. R. Murthy. 2002. Structure of the *Plasmodium falciparum* triosephosphate isomerase-phosphoglycolate complex in two crystal forms: characterization of catalytic loop open and closed conformations in the ligand-bound state. *Biochemistry.* 41:13178–13188.
13. Rozovsky, S., and A. E. McDermott. 2001. The time scale of the catalytic loop motion in triosephosphate isomerase. *J. Mol. Biol.* 310:259–270.
14. Kurkcuoglu, O., R. L. Jernigan, and P. Doruker. 2006. Loop motions of triosephosphate isomerase observed with elastic networks. *Biochemistry.* 45:1173–1182.
15. Skliros, A., M. T. Zimmermann, …, R. L. Jernigan. 2012. The importance of slow motions for protein functional loops. *Phys. Biol.* 9:014001.
16. Zimmermann, M. T., and R. L. Jernigan. 2012. Protein loop dynamics are complex and depend on the motions of the whole protein. *Entropy (Basel).* 14:687–700.
17. Kurkcuoglu, Z., A. Bakan, …, P. Doruker. 2012. Coupling between catalytic loop motions and enzyme global dynamics. *PLOS Comput. Biol.* 8:e1002705.
18. Téllez-Valencia, A., V. Olivares-Illana, …, A. Gómez-Puyou. 2004. Inactivation of triosephosphate isomerase from *Trypanosoma cruzi* by an agent that perturbs its dimer interface. *J. Mol. Biol.* 341:1355–1365.
19. Olivares-Illana, V., R. Pérez-Montfort, …, A. Gómez Puyou. 2006. Structural differences in triosephosphate isomerase from different species and discovery of a multitrypanosomatid inhibitor. *Biochemistry.* 45:2556–2560.
20. Papadopoulou, M. V., W. D. Bloomer, …, J.-R. Ioset. 2013. Novel 3-nitro-1H-1,2,4-triazole-based piperazines and 2-amino-1,3-benzothiazoles as antichagasic agents. *Bioorg. Med. Chem.* 21:6600–6607.
21. Espinoza-Fonseca, L. M., and J. G. Trujillo-Ferrara. 2004. Exploring the possible binding sites at the interface of triosephosphate isomerase dimer as a potential target for anti-tripanosomal drug design. *Bioorg. Med. Chem. Lett.* 14:3151–3154.
22. Espinoza-Fonseca, L. M., and J. G. Trujillo-Ferrara. 2005. Structural considerations for the rational design of selective anti-trypanosomal agents: the role of the aromatic clusters at the interface of triosephosphate isomerase dimer. *Biochem. Biophys. Res. Commun.* 328:922–928.
23. Kurkcuoglu, Z., G. Ural, …, P. Doruker. 2011. Blind dockings of benzothiazoles to multiple receptor conformations of triosephosphate isomerase from *Trypanosoma cruzi* and human. *Mol. Inform.* 30:986–995.
24. Case, D. A., T. A. Darden, …, P. A. Kollman. 2006. AMBER 9. University of California, San Francisco.
25. Duan, Y., C. Wu, …, P. Kollman. 2003. A point-charge force field for molecular mechanics simulations of proteins based on condensed-phase quantum mechanical calculations. *J. Comput. Chem.* 24:1999–2012.
26. Frisch, M. J., G. W. Trucks, …, J. A. Pople. 2004. Gaussian 03, revision D.01. Gaussian, Inc., Wallingford, CT.
27. Berman, H. M., J. Westbrook, …, P. E. Bourne. 2000. The Protein Data Bank. *Nucleic Acids Res.* 28:235–242.
28. Jorgensen, W. L., J. Chandrasekhar, …, M. L. Klein. 1983. Comparison of simple potential functions for simulating liquid water. *J. Chem. Phys.* 79:926–935.
29. Berendsen, H. J. C., J. P. M. Postma, …, J. R. Haak. 1984. Molecular dynamics with coupling to an external bath. *J. Chem. Phys.* 81:3684–3690.
30. Ryckaert, J. P., G. Ciccotti, and H. J. C. Berendsen. 1977. Numerical integration of the Cartesian equations of motion of a system with constraints: molecular dynamics of n-alkanes. *J. Comput. Phys.* 23:327–341.
31. Essman, U., L. Perera, …, L. G. Pedersen. 1995. A smooth particle mesh Ewald method. *J. Chem. Phys.* 103:8577–8593.
32. Amadei, A., A. B. M. Linssen, and H. J. C. Berendsen. 1993. Essential dynamics of proteins. *Proteins.* 17:412–425.
33. Feig, M., J. Karanicolas, III, and C. L. Brooks. 2001. MMTSB Tool Set. MMTSB NIH Research Resource, Scripps Research Institute, La Jolla, CA.
34. Kurkcuoglu, O., O. T. Turgut, …, P. Doruker. 2009. Focused functional dynamics of supramolecules by use of a mixed-resolution elastic network model. *Biophys. J.* 97:1178–1187.
35. Atilgan, A. R., S. R. Durell, …, I. Bahar. 2001. Anisotropy of fluctuation dynamics of proteins with an elastic network model. *Biophys. J.* 80:505–515.

36. Doruker, P., A. R. Atilgan, and I. Bahar. 2000. Dynamics of proteins predicted by molecular dynamics simulations and analytical approaches: application to a-amylase inhibitor. *Proteins.* 40:512–524.

37. Burley, S. K., and G. A. Petsko. 1985. Aromatic-aromatic interaction: a mechanism of protein structure stabilization. *Science.* 229:23–28.

38. Balsera, M. A., W. Wriggers, …, K. Schulten. 1996. Principal component analysis and long time protein dynamics. *J. Phys. Chem.* 100:2567–2572.

39. Hess, B. 2000. Similarities between principal components of protein dynamics and random diffusion. *Phys. Rev. E Stat. Phys. Plasmas Fluids Relat. Interdiscip. Topics.* 62 (6 Pt B):8438–8448.

40. Hess, B. 2002. Convergence of sampling in protein simulations. *Phys. Rev. E Stat. Nonlin. Soft Matter Phys.* 65:031910.

41. Faraldo-Gomez, J. D., L. R. Forrest, …, M. S. P. Samsom. 2004. Conformational sampling and dynamics of membrane proteins from 10-nanosecond computer simulations. *Proteins.* 57:783–791.

42. Grossfield, A., S. E. Feller, and M. C. Pitman. 2007. Convergence of molecular dynamics simulations of membrane proteins. *Proteins.* 67:31–40.

43. Bahar, I., T. R. Lezon, …, E. Eyal. 2010. Global dynamics of proteins: bridging between structure and function. *Annu. Rev. Biophys.* 39:23–42.

44. Romo, T. D., and A. Grossfield. 2011. Validating and improving elastic network models with molecular dynamics simulations. *Proteins.* 79:23–34.

45. Massi, F., C. Wang, and A. G. Palmer, 3rd. 2006. Solution NMR and computer simulation studies of active site loop motion in triosephosphate isomerase. *Biochemistry.* 45:10787–10794.

46. Joseph, D., G. A. Petsko, and M. Karplus. 1990. Anatomy of a conformational change: hinged "lid" motion of the triosephosphate isomerase loop. *Science.* 249:1425–1428.

47. Kempf, J. G., J. Y. Jung, …, J. P. Loria. 2007. Dynamic requirements for a functional protein hinge. *J. Mol. Biol.* 368:131–149.

48. Katebi, A. R., and R. L. Jernigan. 2014. The critical role of the loops of triosephosphate isomerase for its oligomerization, dynamics, and functionality. *Protein Sci.* 23:213–228.

49. Humphrey, W., A. Dalke, and K. Schulten. 1996. VMD: visual molecular dynamics. *J. Mol. Graph.* 14:33–38, 27–28.

50. Jin, L., W. Wang, and G. Fang. 2014. Targeting protein-protein interaction by small molecules. *Annu. Rev. Pharmacol. Toxicol.* 54:435–456.

51. Villoutreix, B. O., M. A. Kuenemann, …, M. A. Miteva. 2014. Drug-like protein-protein interaction modulators: challenges and opportunities for drug discovery and chemical biology. *Mol. Inform.* 33:414–437.

52. Ma, B., and R. Nussinov. 2014. Druggable orthosteric and allosteric hot spots to target protein-protein interactions. *Curr. Pharm. Des.* 20:1293–1301.

53. Nussinov, R., C. J. Tsai, and P. Csermely. 2011. Allo-network drugs: harnessing allostery in cellular networks. *Trends Pharmacol. Sci.* 32:686–693.

**SUPPORTING MATERIAL**

How an inhibitor bound to subunit interface alters triosephosphate isomerase dynamics.

Zeynep Kurkcuoglu[1], Doga Findik[1], Ebru Demet Akten[2], Pemra Doruker[1*]

[1] Department of Chemical Engineering and Polymer Research Center, Bogazici University Bebek, 34342, Istanbul, Turkey

[2] Department of Bioinformatics and Genetics, Faculty of Engineering and Natural Sciences, Kadir Has University, Cibali, Fatih, 34083 Istanbul, Turkey

*Corresponding author: Tel: +90-212-359-7002
Fax: +90-212-257-5032
E-mail address: doruker@boun.edu.tr (P. Doruker)

## FIGURES

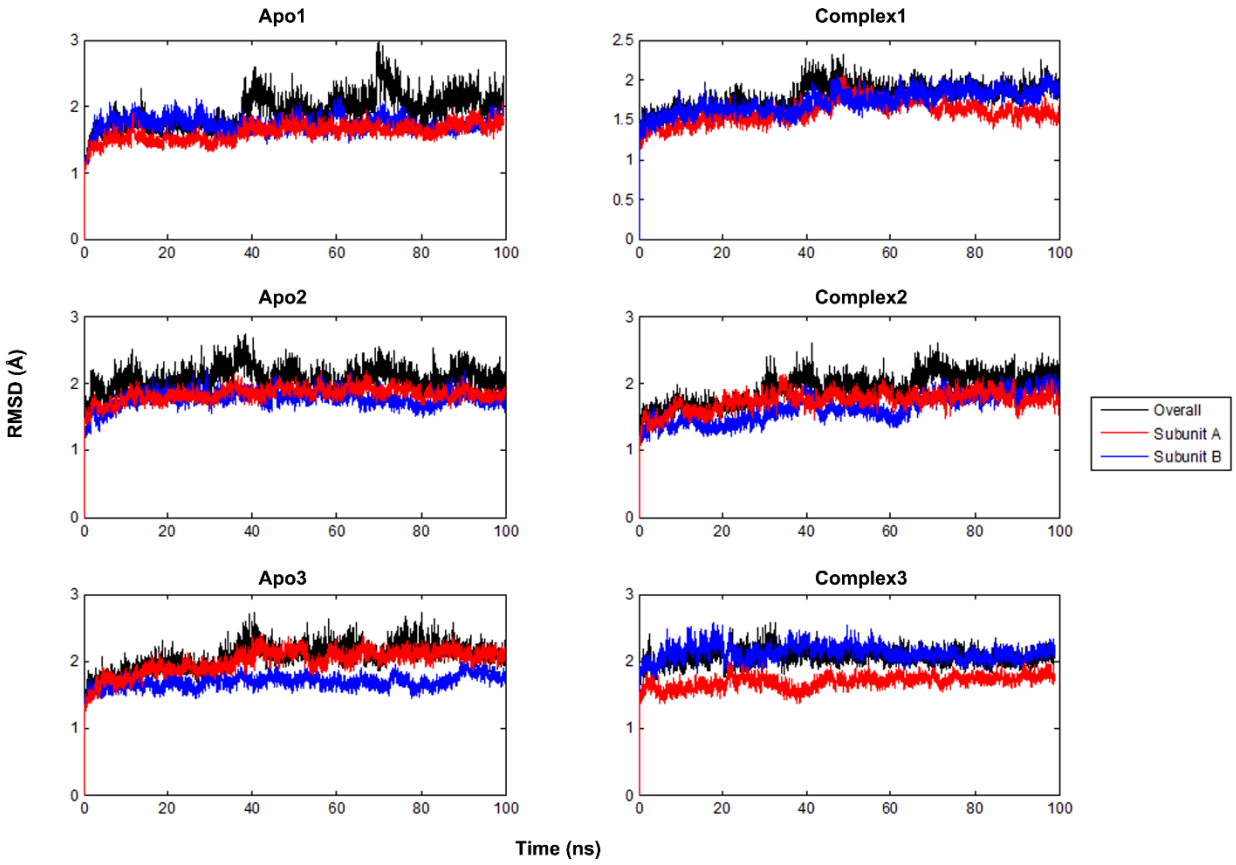


**Figure S1.** Heavy-atom based RMSD profiles for MD runs. RMSDs for each run are calculated after alignment of the snapshots onto its minimized initial structure based on heavy atoms. Overall alignment and RMSD profiles are shown in black. Monomer-based alignment and RMSDs are shown in red (blue) for subunit A (B). Relatively larger deviations in the dimer are indicative of inter-subunit motions.

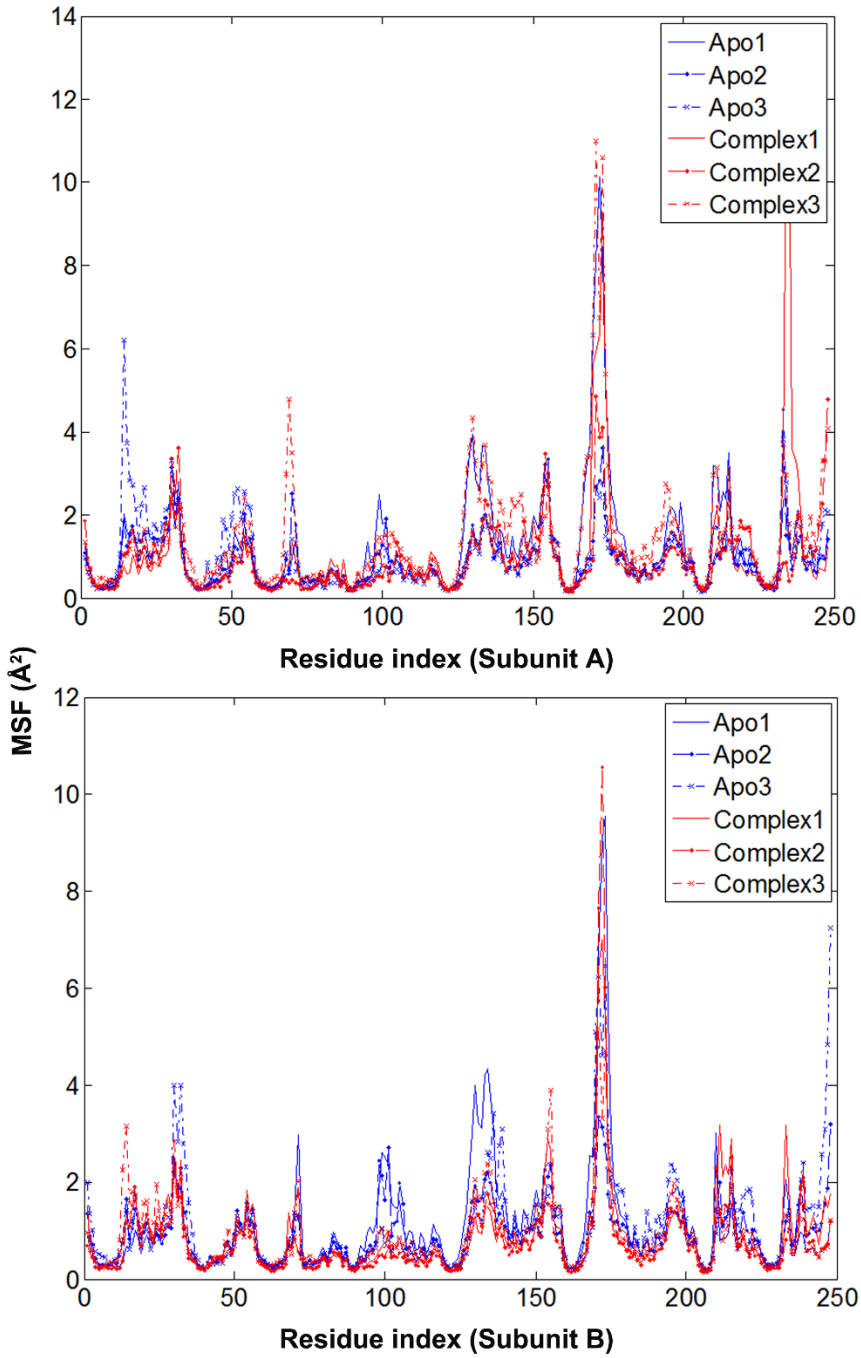


**Figure S2.** Mean square fluctuations (MSF) of apo and complex TIM for each run. We have performed two-way ANOVA to test the null hypothesis that presence of ligand has no effect on residue MSF. Two-way ANOVA revealed that the probability to accept the null hypothesis is 0.0185. Since p-value is less than 0.05, it is statistically significant to reject the null hypothesis, i.e. presence of ligand has effect on residue MSF. Two-way ANOVA is also repeated for individual subunits, yielding p-value of 0.0456 for subunit A and 0.0000 for subunit B, again confirming the effect of bt10 on MSF.

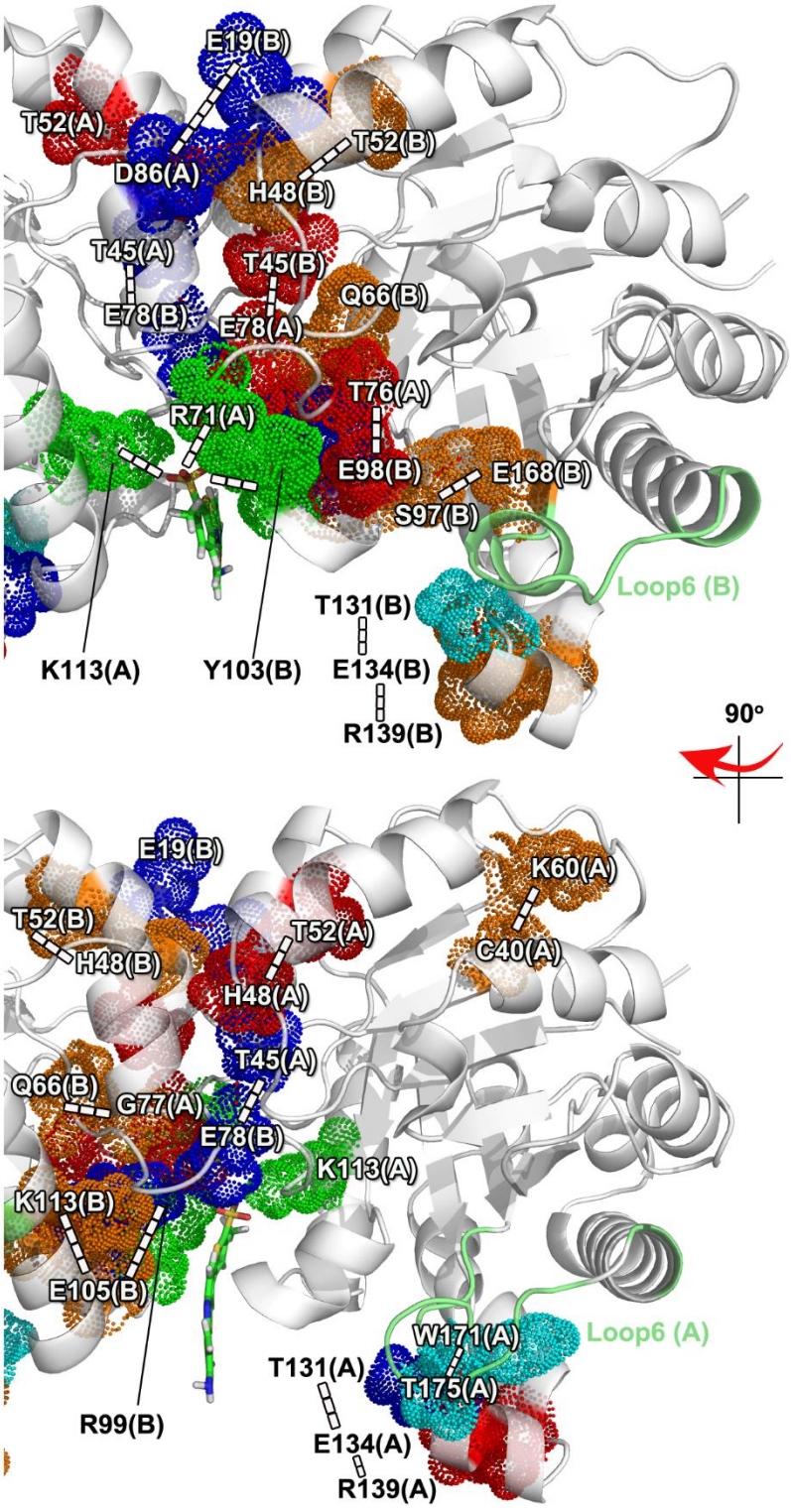


**Figure S3.** Details of the changes in H-bonding network are shown for subunit A (bottom) and B (top). Detailed version of Figure 1-e, where the residue pairs listed in Table S2 are labeled.

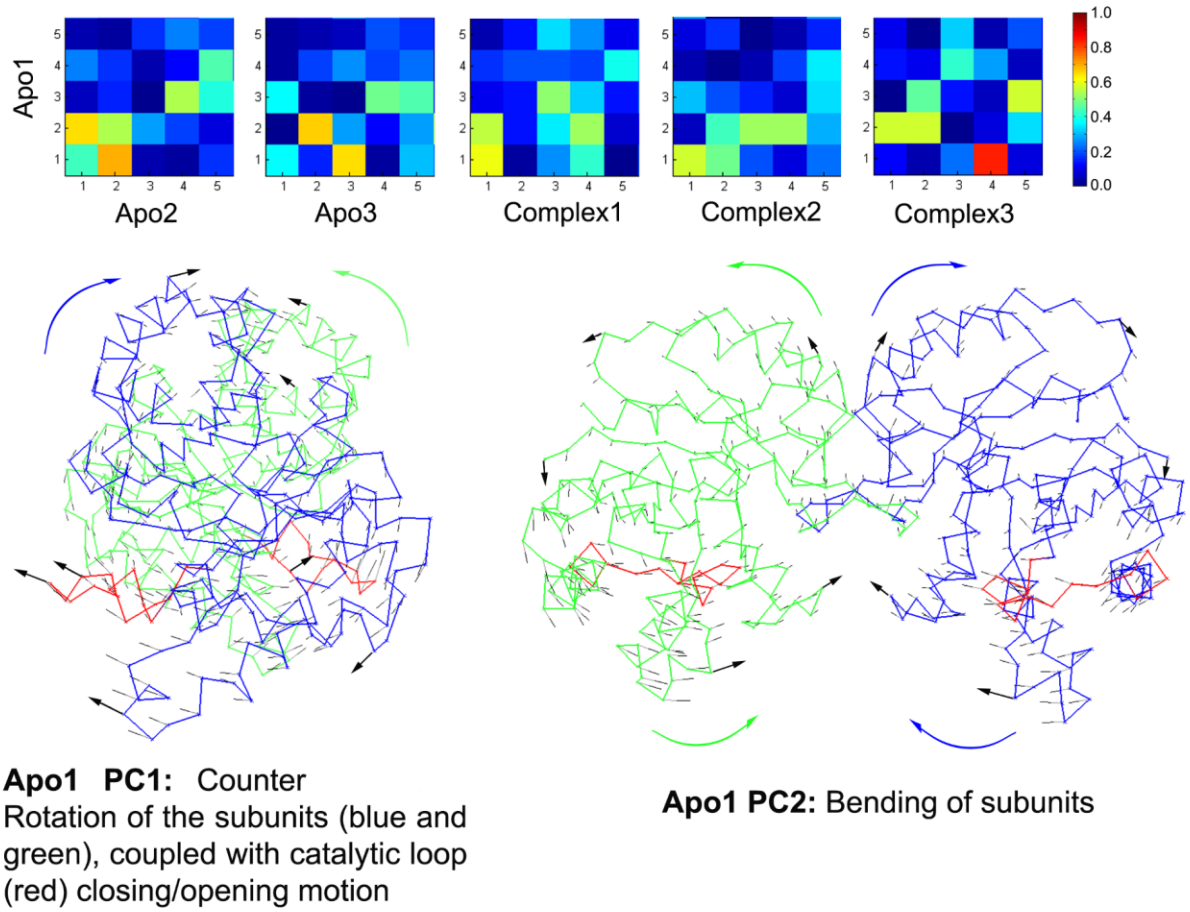


**Figure S4.** PCA mode overlap matrices with reference to Apo1 PCs. Counter rotation of the subunits, coupled with loop 6 opening/closure event over the active site, corresponds to the first PC in Apo1, second in Apo2 and third in Apo3 (side view). This mode is also present in complex simulations, but either with overlap value less than 0.6 (Complex1 and Complex2) or with high overlap but less contribution (Complex3). Contribution of each PC to overall motion is given in Table S3. Another dominant motion is the bending of the subunits (second PC in Apo1), where the lateral movement of the loop 6 is observed (front view). It should be noted that longer runs are necessary for the convergence of essential modes determined by PCA.

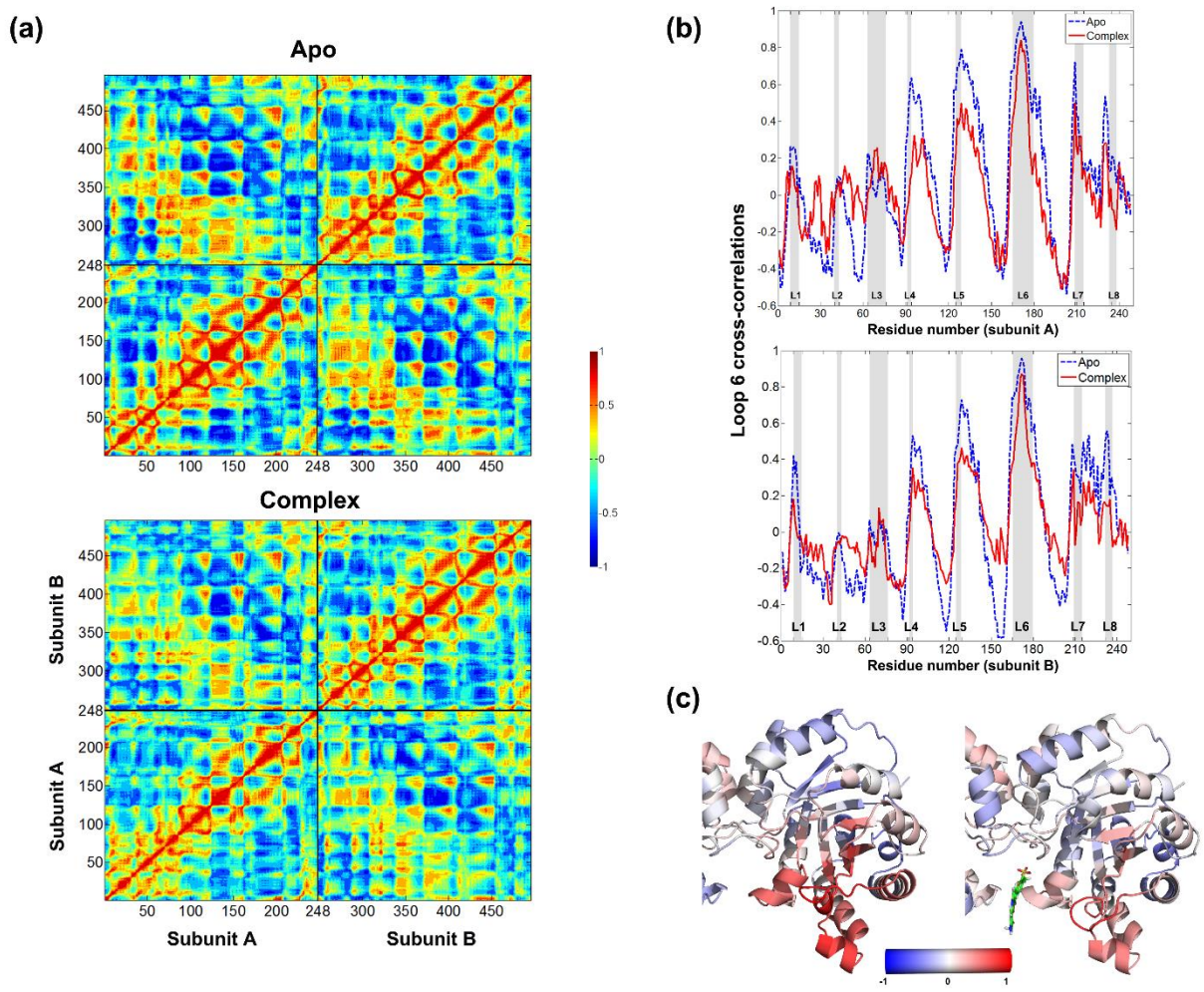


**Figure S5.** Residue-residue orientational cross-correlations based on the cumulative action of first five PCs, reported as averages over three independent runs. (a) Intra- and inter-subunit cross-correlations are shown for apo and complex runs. Presence of inhibitor at the interface often decreases the strength of correlations. (b) Orientational correlations of loop 6 tip residues with other regions, given separately for subunits A and B. This plot represents an average over residues Ile173-Gly174-Thr175, which is based on first five PCs in (a) panels. The ligand decreases the coordination of loop 6 within itself and with other regions including loops 7 and 8. (c) Correlations of loop 6 tip residues color-coded on subunit A for apo and complex simulations (subunit B given in Figure 3-d).

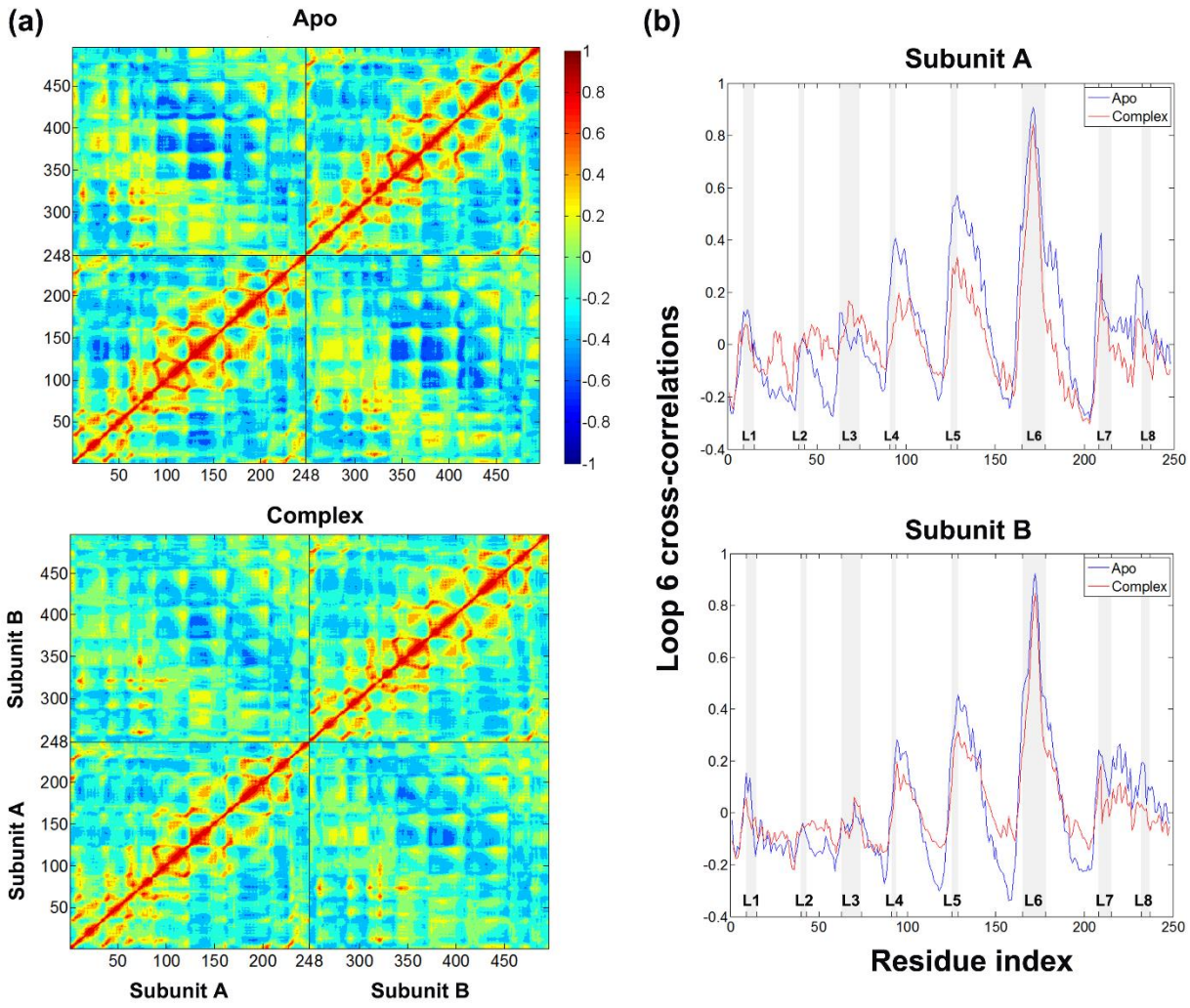


**Figure S6.** Residue-residue orientational cross-correlations based on the cumulative action of the PCs that contribute to 90% of total motion (more than 100 PCs, see Table S3), reported as an average over three independent runs (apo and with ligand). The figure shows a similar trend as in Figure S5 (plotted using the first 5 PCs), for both inter and intra cross-correlations of both subunits and loop 6.

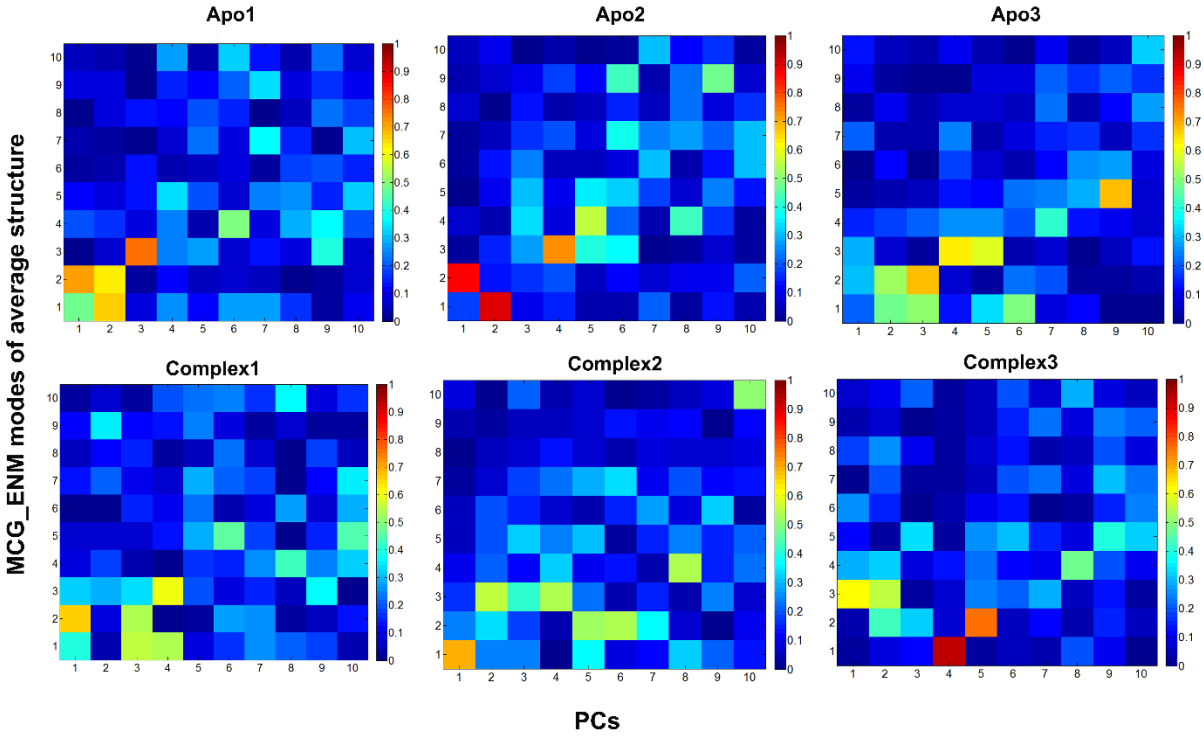


**Figure S7.** Overlap matrices between MCG_ENM modes and PCs plotted for each run. MCG_ENM modes are based on the average structure of each run. Especially the first three ENM modes exhibit an overlap value greater than 0.5 at least with one of the first 5 PCs on the 100 ns timescale. The MCG_ENM takes into account the average structure of the ligand in the complex runs.

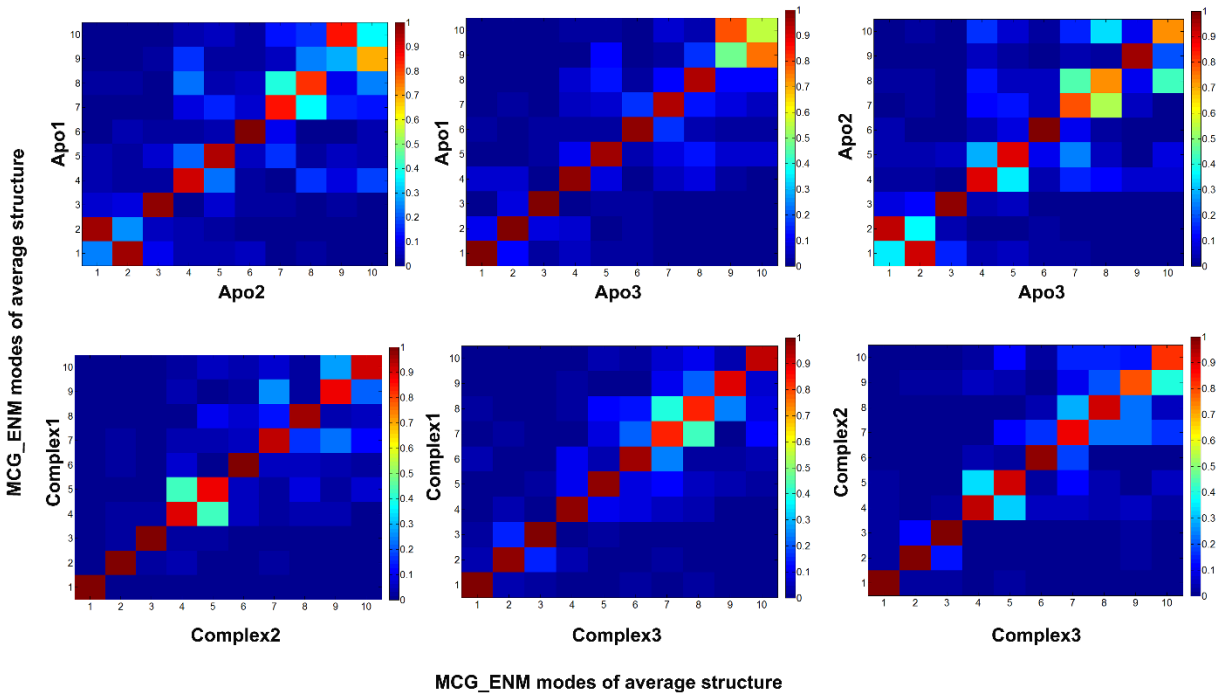


**Figure S8.** Overlap matrices among MCG_ENM modes of different MD runs (based on each run's average structure). Although there is not a one-to-one correspondance between the PCs of apo and complex runs (Figure S4), MCG_ENM modes are fully conserved among apo runs (top panels), as well as complex ones (bottom panels). Therefore, we used MCG_ENM instead of PCA to observe the changes in global modes due to ligand binding, as shown in the next figure.

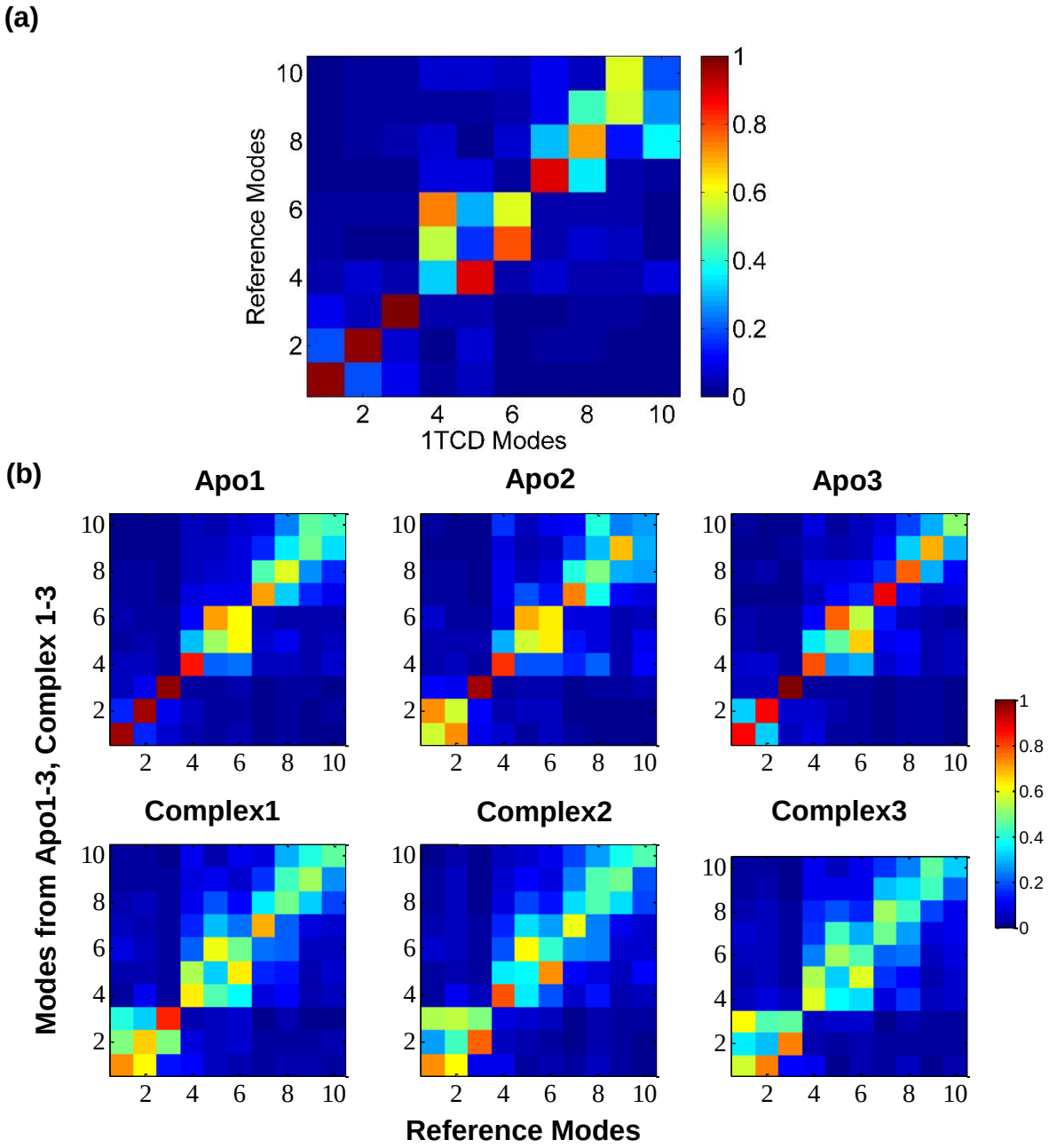


**Figure S9.** Overlap matrices for reference modes (RMs from Apo1 10$^{th}$ ns structure) from MCG_ENM. (a) Overlap matrix between RMs and ENM modes of crystal structure (1tcd). RMs are matching to 1tcd modes, indicating that 10$^{th}$ ns structure of Apo1 is an appropriate choice for reference. (b) Mean overlap matrices between MCG_ENM modes of each snapshot and the reference modes. Average overlap value for each entity is obtained as an average over 9000 frames of a specific run. Figure 2-b in the text presents further averaging over three apo or complex runs (upper/ lower matrices). The RMs are more conservative in apo runs. Issues on mode swapping and change in mode character are given in Table S4.

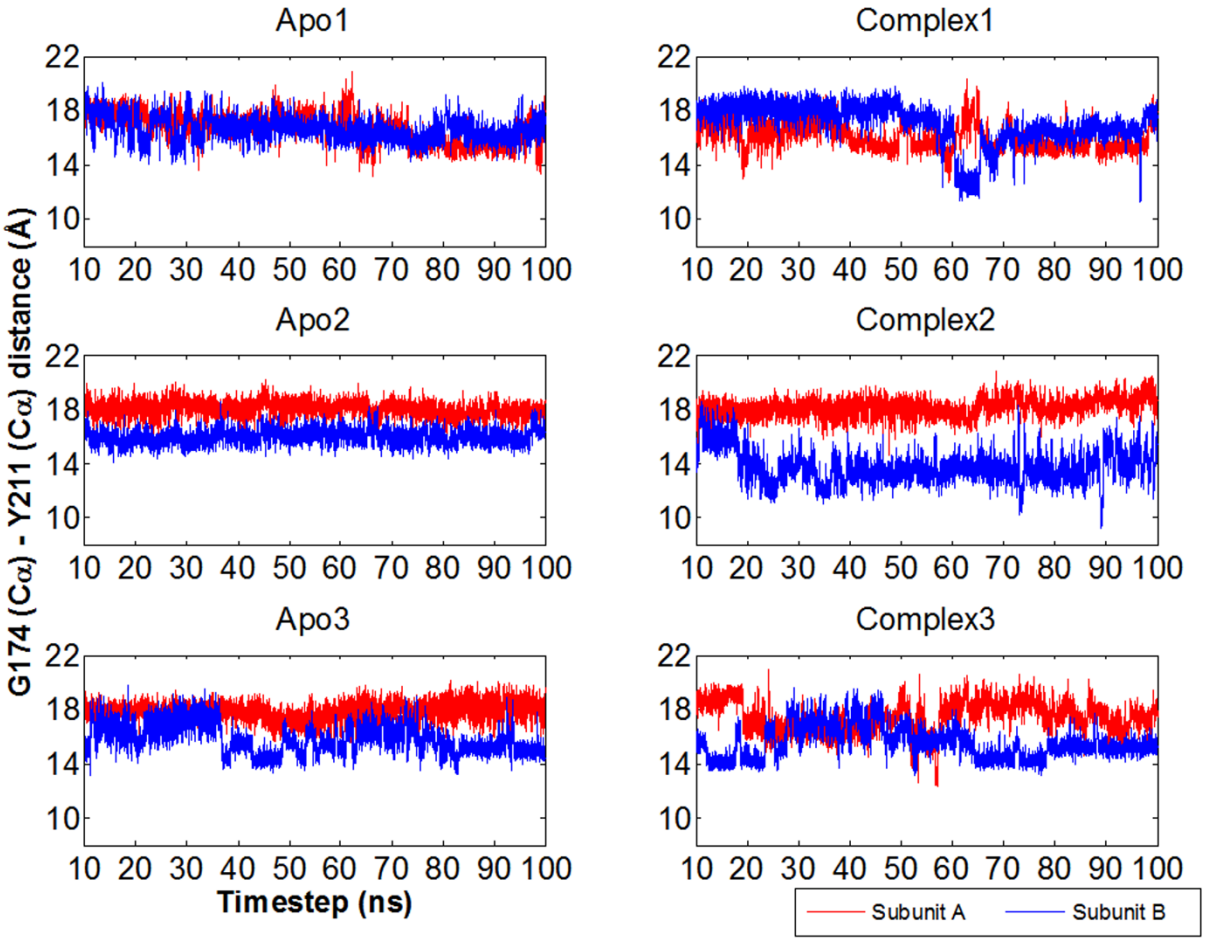


**Figure S10.** Loop 6 opening and closure is observed in the monomers based on the distance between loop's tip residue G174 and a relatively immobile residue Y211. The loop samples lower distances in the complex runs.

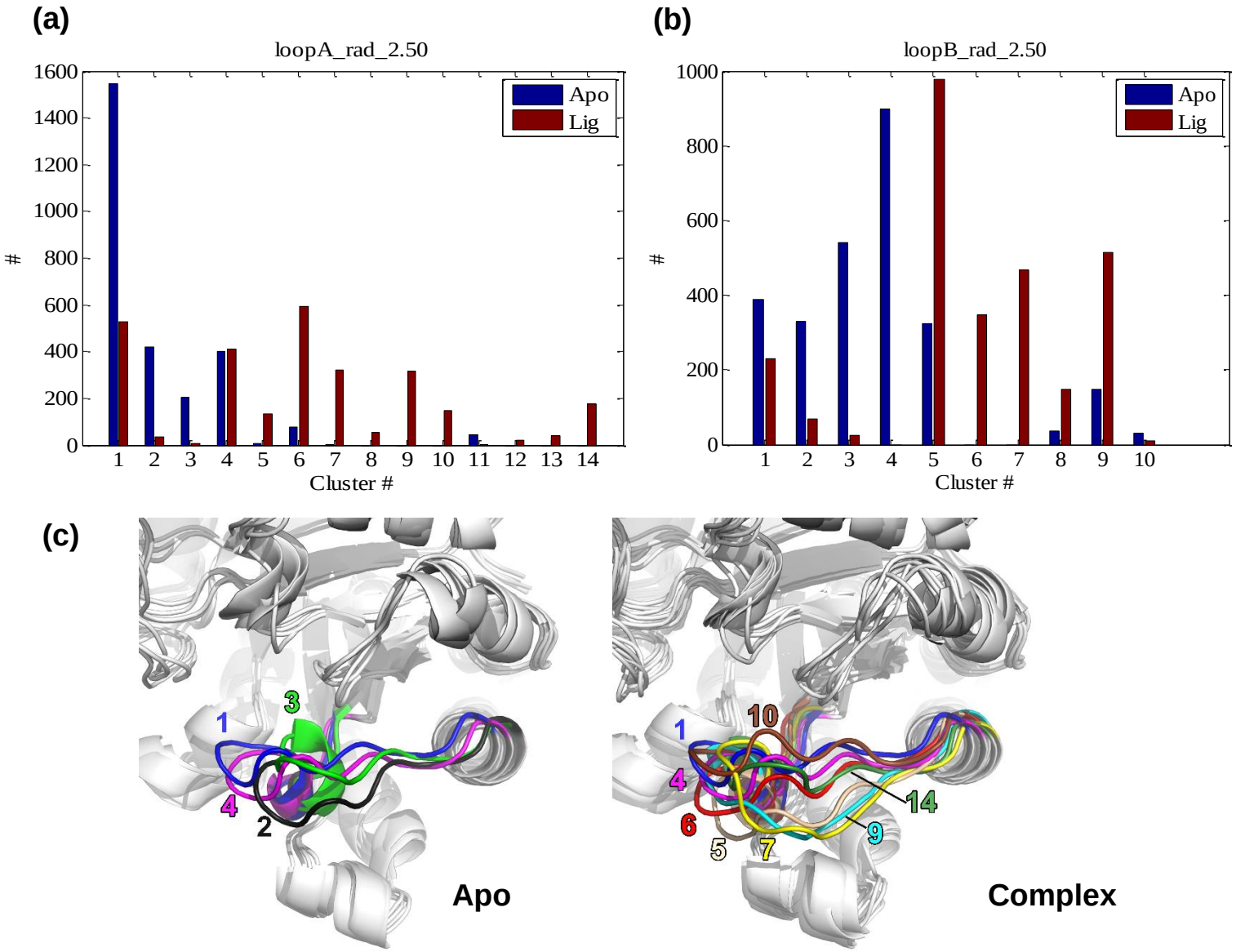


**Figure S11.** Clustering of loop 6 conformers for (a) subunit A and (b) subunit B for apo and complex (over 5400 snapshots in total). Clustering is performed based on mutual RMSD with 2.5 Å cutoff, after alignment of each monomer. (c) Loop 6 clusters sampled in apo and complex simulations for subunit A (see Figure 3-c for subunit B). In both subunits, complex and apo conformers belong to distinct clusters, hinting a causality between inhibitor presence and loop 6 conformational change.

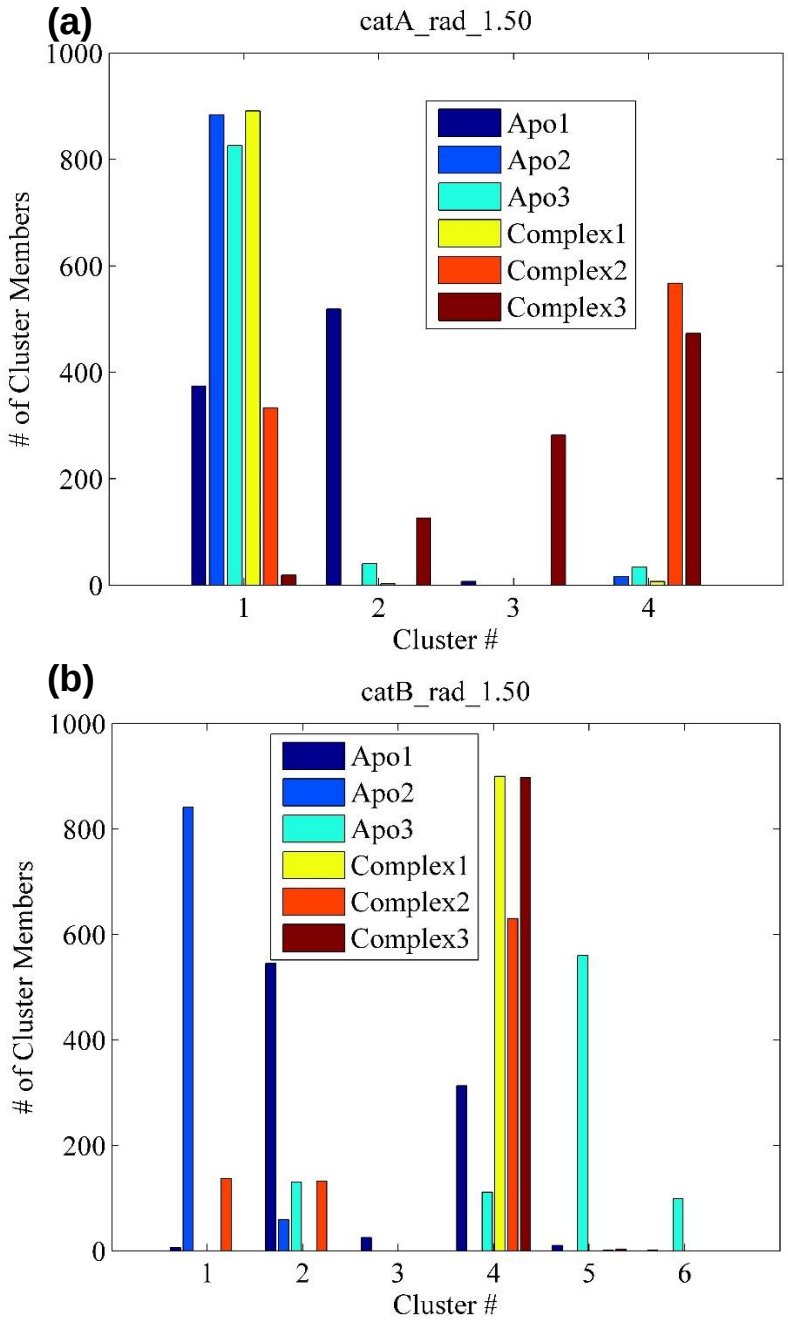


**Figure S12.** Clustering of catalytic residues Asn12, Lys14, His96 and Glu168 for (a) subunit A and (b) subunit B for apo and complex runs (over 5400 snapshots in total). Clustering is performed based on mutual RMSD with 1.5 Å cutoff, after alignment of each monomer. Clusters (presented in Figure 4-b), indicating that apo and complex simulations sample distinct conformers. For subunit B, the complex runs mostly fall in cluster #4, hinting to a constraining effect on the catalytic residues.

**TABLES**

**Table S1.** System details for MD simulations

| MD runs | Total number of atoms | Number of water molecules | Final box dimensions (Å) | Initial structure[a] |
|---|---|---|---|---|
| **Apo1** | 54980 | 15753 | 89 | 1tcd |
| **Apo2** | 54830 | 15711 | 89 | 2 ns of Apo1 |
| **Apo3** | 57554 | 16611 | 90 | 11 ns of Apo1 |
| **Complex1** | 59274 | 17170 | 91 | D1 (1) |
| **Complex2** | 61282 | 17842 | 92 | D3 (1) |
| **Complex3** | 59848 | 17364 | 91 | 0.5 ns of Complex2 |

[a]Apo1 simulation started from the x-ray structure with pdb id 1tcd at 1.83 Å resolution. Initial structures for Apo2 and Apo3 simulations were taken as Apo1 snapshots at 2 and 11 ns, respectively. For TcTIM-bt10 complex simulations, we used bt10-docked structures from our previous docking study (1), which were named as "D1" (7 ns of Apo1, bt10 docked) and "D3" (13.5 ns of Apo1, bt10 docked) in that study and used as initial structures for Complex1 and Complex2, respectively. For Complex3, we used the snapshot at 0.5 ns of Complex2 as initial structure.

**Table S2.** Occurrence percentage of H-bonding residue pairs[a] that differ by more than 15% between apo and complex runs

| Donor Residue | Acceptor Residue | Apo | Complex | Color |
|---|---|---|---|---|
| **Glu19 (B) Main** | **Asp86 (A) Side** | **37** | **13** | **Blue** |
| Cys40 (A) Main | Lys60 (A) Main | 7 | 24 | Orange |
| **Thr45 (B) Side** | **Glu78 (A) Main** | **12** | **44** | **Red** |
| **Thr45 (A) Side** | **Glu78 (B) Main** | **35** | **12** | **Blue** |
| Thr52 (B) Side | His48 (B) Main | 35 | 51 | Orange |
| Thr52 (A) Side | His48 (A) Main | 31 | 53 | Red |
| **Thr76 (A) Side** | **Glu98 (B) Side** | **55** | **81** | **Red** |
| **Gly77 (A) Main** | **Gln66 (B) Side** | **28** | **46** | **Orange** |
| Ser97 (B) Side | Glu168 (B) Side | 38 | 57 | Orange |
| Arg99 (B) Side | Glu105 (B) Side | 43 | 6 | Blue |
| Lys113 (B) Side | Glu105 (B) Side | 26 | 42 | Orange |
| Thr131 (A) Side | Glu134 (A) Side | 49 | 14 | Blue |
| Thr131 (B) Side | Glu134 (B) Side | 36 | 16 | Cyan |
| Arg139 (A) Side | Glu134 (A) Side | 17 | 44 | Red |
| Arg139 (B) Side | Glu134 (B) Side | 24 | 39 | Orange |
| Thr175 (A) Side | Trp171 (A) Main | 35 | 17 | Cyan |

[a]H-bonding pairs are extracted using VMD Hydrogen Bonds analysis, where the default criterion of 3 Å distance between donor and acceptor and 20$^{o}$ supplementary angle is used. Inter-subunit H-bonds are highlighted in bold.

**Table S3.** Individual and cumulative contributions of PCs to total motion

| MD runs | PC1 | PC2 | PC3 | PC4 | PC5 | Cumulative contribution of first 5 PCs | # of PCs that explain 90% of motion |
|---|---|---|---|---|---|---|---|
| **Apo1** | 36.5 | 9.5 | 7.5 | 3.6 | 3.0 | 60 | 100 |
| **Apo2** | 17.0 | 15.6 | 6.6 | 5.0 | 4.0 | 48 | 139 |
| **Apo3** | 19.9 | 13.7 | 9.1 | 5.3 | 4.2 | 52 | 122 |
| **Complex1** | 21.2 | 14.5 | 6.0 | 3.9 | 3.0 | 49 | 134 |
| **Complex2** | 17.6 | 9.0 | 7.1 | 5.4 | 3.9 | 43 | 153 |
| **Complex3** | 27.2 | 10.5 | 6.6 | 5.1 | 4.0 | 53 | 109 |

**Table S4.** Conservation of RMs in MD snapshots using MCG_ENM

| **RM Index**[a] | **% of mode shape conservation**[b] | | **% of mode index conservation**[c] | |
|---|---|---|---|---|
| | Apo | Complex | Apo | Complex |
| 1 | 98 | 74 | 70 | 47 |
| 2 | 99 | 71 | 70 | 21 |
| 3 | 100 | 99 | 100 | 50 |
| 4 | 94 | 73 | 85 | 54 |
| 5 | 87 | 69 | 11 | 0 |
| 6 | 64 | 53 | 16 | 3 |
| 7 | 91 | 67 | 78 | 46 |
| 8 | 58 | 33 | 45 | 17 |
| 9 | 67 | 41 | 52 | 24 |
| 10 | 13 | 11 | 11 | 10 |

[a] RMs are the reference ENM modes obtained from the 10$^{th}$ ns snapshot Apo1 run.

[b] The percentage of MD snapshots that present at least one ENM mode (among its first 10 modes) that highly correlates (overlap > 0.7) with a specific RM is reported for apo and complex runs. Through this calculation, changes in mode shapes can be detected because mode swapping is not considered. First four modes are almost always present in apo simulations. However, with bound-bt10, RM1, RM2 and RM4 change character in 25-30 % of the snapshots but RM3 is preserved.

[c] The percentage of MD snapshots that preserve both the mode shape (overlap > 0.7) and the mode index are reported with reference to each RM. The extent of mode swapping can be inferred from these numbers.

## References


1. Kurkcuoglu, Z., G. Ural, D. Akten, and P. Doruker. 2011. Blind Dockings of Benzothiazoles to Multiple Receptor Conformations of Triosephosphate Isomerase from *Trypanosoma cruzi* and human. Mol. Inf. 30:986 – 995.